FABRICATION OF ANNEALED PROTON-EXCHANGED WAVEGUIDES VERTICALLY INTEGRATED WITH CHALCOGENIDE WAVEGUIDES

A Thesis

by

DWAYNE DENTON MACIK

Submitted to the Office of Graduate Studies of
Texas A&M University
in partial fulfillment of the requirements for the degree of

MASTER OF SCIENCE

August 2012

Major Subject: Electrical Engineering

Fabrication of Annealed Proton-Exchanged Waveguides Vertically Integrated with Chalcogenide Waveguides

FABRICATION OF ANNEALED PROTON-EXCHANGED WAVEGUIDES VERTICALLY INTEGRATED WITH CHALCOGENIDE WAVEGUIDES

A Thesis

by

DWAYNE DENTON MACIK

Submitted to the Office of Graduate Studies of
Texas A&M University
in partial fulfillment of the requirements for the degree of

MASTER OF SCIENCE

Approved by:

Chair of Committee,	Christi K. Madsen
Committee Members,	Ohannes Eknoyan
	Jim Ji
	Kenith Meissner
Head of Department,	Costas Georghiades

August 2012

Major Subject: Electrical Engineering

ABSTRACT

Fabrication of Annealed Proton-Exchanged Waveguides Vertically Integrated with Chalcogenide Waveguides. (August 2012)

Dwayne Denton Macik, B.S., Texas A&M University

Chair of Advisory Committee: Dr. Christi K. Madsen

A key factor in the vertical integration of optical waveguide devices is the uniformity of the surface across which the coupling takes place. This thesis focuses on the fabrication of annealed proton-exchanged (APE) waveguides vertically integrated with chalcogenide waveguides. While titanium diffused waveguides form a surface bump that is approximately twice the size of the originally deposited film, an annealed proton-exchange process produces waveguides with surfaces having 90% less deformation.

The theory behind wave guiding devices is explored in this work along with the modeling and simulation of APE waveguides. The results obtained from the simulations are used to aid in the fabrication of these devices. A detailed review of the fabrication process of APE waveguides and chalcogenide waveguides is provided with results obtained from measurements. The first known coupling results for vertically integrated chalcogenide waveguides on top of annealed proton-exchanged waveguides are recorded. This work is concluded with future directions for this research including

lowering losses by obtaining better simulation parameters and vertically integrating ring resonators along with ways in which to do this.

To my family

ACKNOWLEDGEMENTS

I would like to thank my committee chair and advisor, Dr. C.K. Madsen, for the opportunity she has given me to pursue an advanced degree and the knowledge and guidance she has provided along the way. I would also like to acknowledge Dr. Ohannes Eknoyan, Dr. Jim Ji, and Dr. Kenith Meissner for being on my committee and for also offering any advice when needed. I thank Jacob Webb for passing his knowledge to me and for training me in the fabrication process. I thank Tim Snider for being a mentor and a friend. I also would like to thank the rest of the Photonic Signal Processing research group: Ran Huang, Ivan Yifeng Zhou, Cage Qi Chen, Xin Wang, and Jae Kim for all their help and friendships.

I thank my mom and my dad for always encouraging and believing in me and for teaching me to set my goals high and never give up. I thank my sister for her support and encouragement. Lastly, I thank Maria for always being there and for all her love.

TABLE OF CONTENTS

CHAPTER Page

Page

LIST OF FIGURES

FIGURE Page

FIGURE Page

LIST OF TABLES

CHAPTER I

INTRODUCTION

A. Background

As more electronic devices become connected to the internet, it is essential to match the increase in user demands with larger bandwidth and faster speeds. To meet these demands, high speed telecommunications systems through optical fibers have become predominant, along with the interest in the field of integrated optics. This is because these devices not only offer faster speeds and communication over long distances, but also provide higher bandwidth and are easily interfaced with pre-existing fiber optic systems. Devices such as amplitude and phase modulators, Mach-Zehnder interferometers, and ring resonators can be fabricated on these optical chips. By incorporating these devices and various other components onto a single chip, systems effectively become more efficient and reduced in size. This work focuses on the fabrication of low-loss annealed proton exchange (APE) waveguides and the fabrication of chalcogenide waveguides for vertical integration with APE waveguides.

To accomplish the goals of this research, one needs to simply create a refractive index change in the $LiNbO_3$ so that light can be guided and coupled into the chalcogenide waveguides to create optical modulators and filters. With this, feed-forward Mach-Zehnder interferometers (MZI), and feed-back ring resonators can be

---

This thesis follows the style of *IEEE Journal of Lightwave Technology*.

devised as seen in Fig. 1. The MZI is a two-path structure that divides the incoming light into each respective path. Because the path length and/or refractive index are different for each branch, constructive and destructive interference occurs at the recombination point. This results in phase and amplitude modulation. Two of the main processes by which to create this index change is the indiffusion of titanium [1] or the exchange of a proton (H^+) source such as benzoic acid (C_6H_5COOH) [2], into the lithium niobate.

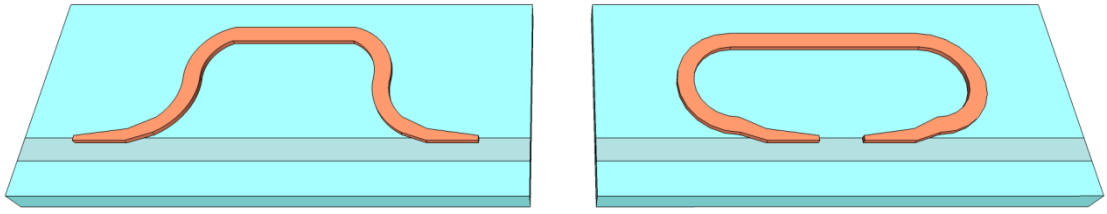

(a) (b)

Fig. 1 a) MZI and b) Ring resonator structures

B. Organization

This thesis is organized in chapters that help develop an understanding of how these waveguides are fabricated. The following sections include the theory that drives this research, the fabrication process, and measurements/results obtained with the devices that have been fabricated.

Chapter 1 includes a short introduction of the driving force behind this research. It also gives the organization of this thesis.

Chapter 2 explains some of the relevant properties of the lithium niobate ($LiNbO_3$) substrate used and the theory behind optical waveguides. Step-index, diffused, and ridge waveguides are also explained, as well as the vertical integration of the diffused and ridge waveguides.

Chapter 3 is an in depth analysis of the APE process, which includes background behind its development and the modeling of this type of wave guiding structure with different computer assisted programs.

Chapter 4 is dedicated to the fabrication process of this device. It will include the processes from dicing to polishing and from photolithography to proton exchange with the trials associated with each individual process and how low-loss optical waveguides are produced.

Chapter 5 includes measurements and results that have been obtained. Characteristics of straight APE waveguides are examined, including their losses, mode profiles, and index changes. Vertically integrated APE and chalcogenide waveguides are subsequently characterized.

Chapter 6 consists of a conclusion to the research of this thesis and also contains future realizations of vertically integrated APE and chalcogenide waveguides.

CHAPTER II

DEVICE THEORY

A. Wave Theory in Dielectric Waveguides

The differential form of Maxwell's equations in a time varying situation written in terms of the electric field **E** (V/m), magnetic flux density **B** (Wb/m^2), magnetic field **H** (A/m), and electric flux density, **D** (C/m^2), are given by [3]

$$\nabla \times \mathbf{E} = -\frac{\partial \mathbf{B}}{\partial t} \tag{1}$$

$$\nabla \times \mathbf{H} = \mathbf{J} + \frac{\partial \mathbf{D}}{\partial t} \tag{2}$$

$$\nabla \cdot \mathbf{D} = \rho_v \tag{3}$$

$$\nabla \cdot \mathbf{B} = 0 \tag{4}$$

where ρ_v is the volume density of free charges and **J** is the density of free currents. When in a lossless source-free nonconducting medium (1)-(4) reduce to

$$\nabla \times \mathbf{E} = -\mu \frac{\partial \mathbf{H}}{\partial t} \tag{5}$$

$$\nabla \times \mathbf{H} = \varepsilon \frac{\partial \mathbf{E}}{\partial t} \tag{6}$$

$$\nabla \cdot \mathbf{E} = 0 \tag{7}$$

$$\nabla \cdot \mathbf{H} = 0 \tag{8}$$

where ε and μ are the electric permittivity and magnetic permeability of the medium, respectively. It can be seen that (5)-(8) are first-order differential equations related by the electric and magnetic fields. By taking the curl of (5) and using (6) it becomes

$$\nabla\times\nabla\times\mathbf{E}=-\mu\frac{\partial}{\partial t}\left(\nabla\times\mathbf{H}\right)=-\mu\varepsilon\frac{\partial^2\mathbf{E}}{\partial t^2}\ . \tag{9}$$

Given that $\nabla\times\nabla\times\mathbf{E}=\nabla\left(\nabla\cdot\mathbf{E}\right)-\nabla^2\mathbf{E}=-\nabla^2\mathbf{E}$ because of (7), (9) becomes

$$\nabla^2\mathbf{E}-\mu\varepsilon\frac{\partial^2\mathbf{E}}{\partial t^2}=0\ . \tag{10}$$

The permittivity, ε, and permeability, μ, are related to their respective free space values ε_0=8.854x10^{-12} [F/m] and μ_0=4πx10^{-7} [H/m], by

$$\varepsilon=\varepsilon_0 n^2 \tag{11}$$

$$\mu=\mu_0 \tag{12}$$

and $u_p=1/\sqrt{\mu\varepsilon}=1/n\sqrt{\mu_0\varepsilon_0}$, therefore,

$$\nabla^2\mathbf{E}-\frac{1}{u_p^2}\frac{\partial^2\mathbf{E}}{\partial t^2}=0\ . \tag{13}$$

This same derivation can be done starting with (6), giving

$$\nabla^2\mathbf{H}-\frac{1}{u_p^2}\frac{\partial^2\mathbf{H}}{\partial t^2}=0\ . \tag{14}$$

Equations (13) and (14) are the homogeneous Helmholtz equations. For optical field solutions, a space and time varying field propagating in the z-direction with propagation constant β can be defined as

$$\mathbf{E}\left(\mathbf{r},t\right)=\mathbf{E}\left(\mathbf{r}\right)\mathbf{e}^{j(\omega t-\beta z)} \tag{15}$$

Solving (13) with (15) and substituting $c = \frac{1}{\sqrt{\mu_0 \varepsilon_0}}$ and $k = \frac{n\omega}{c}$ yields

$$\nabla^2 \mathbf{E} + \left(k^2 - \beta^2\right)\mathbf{E} = 0 \ . \tag{16}$$

The same can be done with the magnetic field and (14) giving

$$\nabla^2 \mathbf{H} + \left(k^2 - \beta^2\right)\mathbf{H} = 0 \ . \tag{17}$$

B. Propagation in Uniaxial Crystals

Lithium niobate ($LiNbO_3$) is the substrate of choice because of its favorable optical, electro-optic, and photorefractive properties, among others [4]. It also has a high ferroelectric Curie temperature (approximately 1210°C) [5] that allows for reasonably fast diffusion times at high temperatures. $LiNbO_3$ is a uniaxial anisotropic crystal [6] that is characterized by the symmetric 3x3 dielectric tensor with axes of an orthogonal coordinate transformed to its principal axes, as follows

$$[\varepsilon] = \begin{bmatrix} \varepsilon_{11} & 0 & 0 \\ 0 & \varepsilon_{22} & 0 \\ 0 & 0 & \varepsilon_{33} \end{bmatrix} . \tag{18}$$

When this dielectric tensor is used with the above mentioned electric field and electric flux density vectors, the relationship is

$$\mathbf{D} = \varepsilon_0 [\varepsilon]\mathbf{E} \ . \tag{19}$$

The electric energy that is stored in a crystal is given by

$$w = \frac{1}{2}\mathbf{E}\cdot\mathbf{D} \tag{20}$$

Substituting equations (18) and (19) into (20), and representing the electric flux density vector **D** in its vector components gives

$$w = \frac{1}{2\varepsilon_0}\left(\frac{D_x^2}{\varepsilon_{11}} + \frac{D_y^2}{\varepsilon_{22}} + \frac{D_z^2}{\varepsilon_{33}}\right) . \tag{21}$$

If $D_i \Big/ \sqrt{2\varepsilon_0 w}$ is replaced with *i*, where *i* = *x*, *y*, *z* and $\varepsilon_{jj} = n_i^2$ equation (21) becomes

$$\frac{x^2}{n_x^2} + \frac{y^2}{n_y^2} + \frac{z^2}{n_z^2} = 1 . \tag{22}$$

This is known as the index ellipsoid and has the principal axes *x*, *y*, and *z*. The radii along the directions of these axes are the principal refractive indices n_x, n_y, and n_z, respectively.

Because $LiNbO_3$ has trigonal crystal structure [7], the index ellipsoid is rotationally symmetric with respect to the z axis, or optical axis. This means that $LiNbO_3$ is optically uniaxial [6] where $n_x = n_y \neq n_z$ ($\varepsilon_{11} = \varepsilon_{22} \neq \varepsilon_{33}$). Moreover, this substrate is a negative uniaxial crystal where $n_x = n_y = n_o$, $n_z = n_e$, and $n_o > n_e$. For the two rays of light present that are orthogonal and linearly-polarized in nature, there is only a single direction in which these two waves see the same refractive index and it is the optical z axis. The first light ray is the ordinary ray and is independent of the angle θ, so it always sees the refractive index n_o. This is evident from the index ellipsoid in Fig. 2. The other ray is known as the extraordinary ray and is dependent on the angle θ. The refractive index seen by the extraordinary ray, $n_e(\theta)$, is

$$\begin{cases} n_e^2(\theta) = y^2 + z^2 \\ z = n_e(\theta) \cdot \sin(\theta) \end{cases} . \tag{23}$$

Equation (22) can now be rewritten as

$$\frac{x^2}{n_o^2} + \frac{y^2}{n_o^2} + \frac{z^2}{n_e^2} = 1 . \tag{24}$$

The substitution of equation (23) into (24) yields

$$n_e(\theta) = \frac{n_e n_o}{\sqrt{n_e^2 \cos^2(\theta) + n_o^2 \sin^2(\theta)}} . \tag{25}$$

From the above equation, it can be seen that the extraordinary wave sees $n_e(\theta) = n_e$ at $\theta = 0°$ to $n_e(\theta) = n_o$ at $\theta = 90°$.

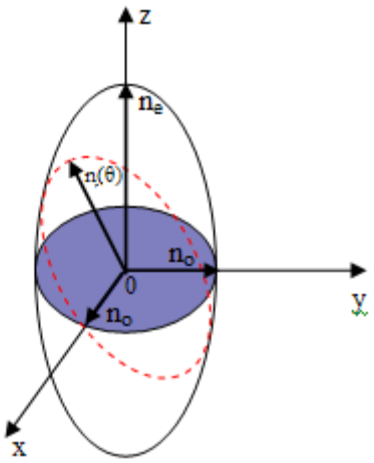

Fig. 2 Index ellipsoid of negative uniaxial crystal.

In x-cut lithium niobate, which is used in this research, the vertically polarized transverse magnetic (TM) mode sees the ordinary index and the horizontally polarized transverse electric (TE) mode sees the extraordinary refractive index. This is visualized in Fig. 3.

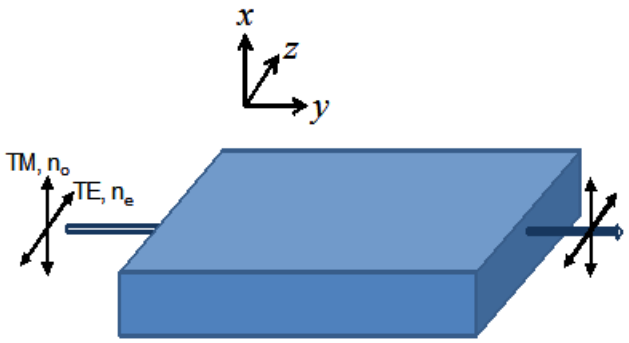

Fig. 3 X-cut y-propagating lithium niobate. The vertically polarized TM mode sees the ordinary index and the horizontally polarized TE mode sees the extraordinary index.

For devices to be designed properly and in order for them to work correctly in the desired spectral area, the wavelength dependent refractive indices must be known. An equation that relates refractive index and wavelength was first put forward by Wolfgang Sellmeier and is known as the Sellmeier dispersion equation. The Sellmeier equation is of the form [8]

$$n^2(\lambda) = 1 + \frac{C_1\lambda^2}{\lambda^2 - C_2} + \frac{C_3\lambda^2}{\lambda^2 - C_4} + \frac{C_5\lambda^2}{\lambda^2 - C_6} \tag{26}$$

where C_i are the Sellmeier coefficients. Extensive research has been carried out on the refractive indices for specific wavelengths [9] and on the temperature dependence of the

indices for various wavelengths [10]. This research is focused on the telecommunications wavelength of 1.531 μm. An infrared corrected Sellmeier equation for the wavelengths from 0.4-5.0 μm has been created [8]. In studies that have used only the single oscillator model of the Sellmeier equation, it has been found that the refractive indices for the respective ends of the spectrum deviate greatly. Therefore, a three oscillator model is used, as in (26), to fit the data from the experiment. This fit produces the Sellmeier coefficients found in Table I.

Table I
Sellmeier Coefficients [10]

Coefficient	n_o	n_e
C_1	2.6734	2.9804
C_2	0.01764	0.02047
C_3	1.2290	0.5981
C_4	0.05914	0.0666
C_5	12.614	8.9543
C_6	474.6	416.08

When these coefficients are used in (26) with the wavelength of 1.531 μm, n_o = 2.21176 and n_e = 2.13811.

Because electro-optic tuning by use of the linear Pockel's effect is outside the scope of this research, it will briefly be discussed here and will be revisited in the future work section of Chapter 6. The linear electro-optic effect is found in crystals, such as $LiNbO_3$, where the refractive index changes linearly with an applied electric field [6]. When discussing the Pockel's effect, it is more convenient to use the impermeability, B

$$B = \frac{1}{\left(\varepsilon/\varepsilon_0\right)} = \frac{1}{n^2} \ . \tag{27}$$

Equation (24) can therefore be expressed as

$$B_{11}x^2 + B_{22}y^2 + B_{33}z^2 + 2B_{23}yz + 2B_{31}zx + 2B_{12}xy = 1 \ . \tag{28}$$

When an electric field is applied, the modified index ellipsoid (28) is written as

$$B_1'x^2 + B_2'y^2 + B_3'z^2 + 2B_4'yz + 2B_5'zx + 2B_6'xy = 1 \ . \tag{29}$$

The impermeability and the electric field vector, $\mathbf{E^e}$, are related through the electro-optic tensor and is expressed as

$$\Delta B_i = B_i' - B_i = \frac{1}{n_i^2} = \sum_{j=1}^{3} r_{ij}E_j \tag{30}$$

where r_{ij} is the electro-optic tensor. Written in matrix form, (30) becomes

$$\begin{bmatrix} \Delta\frac{1}{n_1^2} \\ \Delta\frac{1}{n_2^2} \\ \Delta\frac{1}{n_3^2} \\ \Delta\frac{1}{n_4^2} \\ \Delta\frac{1}{n_5^2} \\ \Delta\frac{1}{n_6^2} \end{bmatrix} = \begin{bmatrix} r_{11} & r_{12} & r_{13} \\ r_{21} & r_{22} & r_{23} \\ r_{31} & r_{32} & r_{33} \\ r_{41} & r_{42} & r_{43} \\ r_{51} & r_{52} & r_{53} \\ r_{61} & r_{62} & r_{63} \end{bmatrix} \begin{bmatrix} E_x^e \\ E_y^e \\ E_z^e \end{bmatrix} \ . \tag{31}$$

In negative uniaxial crystals with trigonal structure, such as $LiNbO_3$, the electro-optic tensor reduces to

$$r_{ij} = \begin{bmatrix} 0 & -r_{22} & r_{13} \\ 0 & r_{22} & r_{13} \\ 0 & 0 & r_{33} \\ 0 & r_{51} & 0 \\ r_{51} & 0 & 0 \\ -r_{22} & 0 & 0 \end{bmatrix} \tag{32}$$

For $LiNbO_3$, the coefficients for the electro-optic tensor are given by [11]

$$r_{ij} = \begin{bmatrix} 0 & -3.4 & 8.6 \\ 0 & 3.4 & 8.6 \\ 0 & 0 & 30.8 \\ 0 & 28 & 0 \\ 28 & 0 & 0 \\ -3.4 & 0 & 0 \end{bmatrix} \; pm/V \tag{33}$$

The refractive indices of the ordinary ray, n_y, and the extraordinary ray, n_z, with an electric field applied along the optical axis are given by

$$\begin{cases} n_y = n_o - \Delta n_o, \quad \Delta n_o = \dfrac{1}{2} r_{13} n_o^3 E_z^e \\ n_z = n_e - \Delta n_e, \quad \Delta n_e = \dfrac{1}{2} r_{33} n_e^3 E_z^e \end{cases} \tag{34}$$

The change in the extraordinary refractive index is critical for x-cut, y-propagating APE waveguides fabricated on $LiNbO_3$. This APE configuration supports the propagation of the TE mode, which sees n_e. As noticed in (34), it will take advantage of the r_{33} electro-optic coefficient, which is the largest for $LiNbO_3$.

C. Step-index Waveguides

A wave guiding region is created by having a higher index contrast material. The simplest structure is a slab planar waveguide which is shown in Fig. 4. To satisfy the wave guiding condition for region n_1, $n_1 > n_2 \geq n_3$. In terms of the propagation constant β this relationship can be expressed as $k_o n_1 > \beta > k_o n_2 \geq k_o n_3$. We can define three constants q, h, p with the form

$$q \equiv \sqrt{\left(\beta^2 - k_o^2 n_1^2\right)} \tag{35}$$

$$h \equiv \sqrt{k_o^2 n_2^2 - \beta^2} \tag{36}$$

$$p \equiv \sqrt{\beta^2 - k_o^2 n_3^2} \tag{37}$$

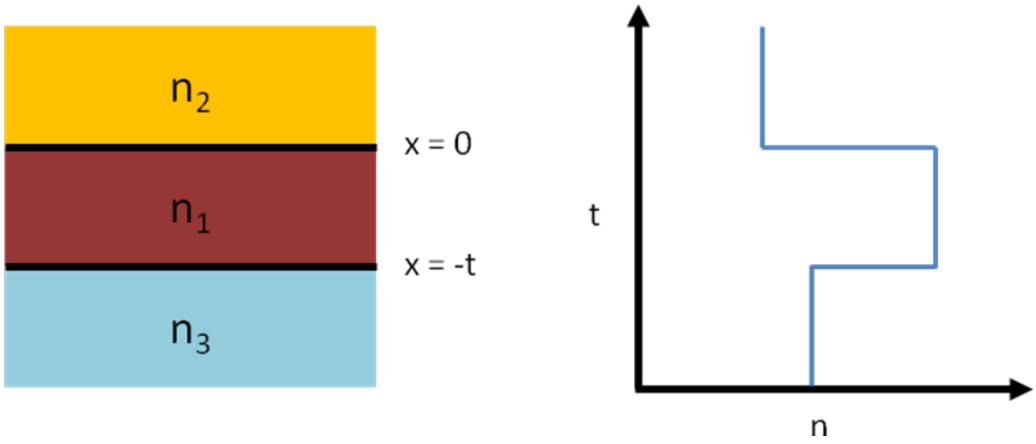

Fig. 4 Planar wave guiding structure. a) Waveguide structure with b) index profile.

For the TE mode (16) has solutions of the form

$$E_y(x) = \begin{cases} Ae^{-qx} & x > 0 \\ B\cos(hx) + C\sin(hx) & 0 \le x \le -t \\ De^{p(x+t)} & x < -t \end{cases} \tag{38}$$

Applying boundary conditions for continuous electric and magnetic fields gives the eigenvalue equation [6]

$$\tan(ht) = \frac{q+p}{h - \frac{qp}{h}} \tag{39}$$

The simplest way to solve this equation is to plot each side individually and find the intercepts as seen in Fig. 5. The number of intersecting points is the number of modes allowed to propagate in the wave guiding region. Because we are plotting against *h*, these intersecting points give us the allowed *h* values. Knowing *h* from (36) and that $\beta = k_o n_{eff}$, we can find the effective index from

$$n_{eff} = \sqrt{n_2^2 - \left(\frac{h}{k_o}\right)^2} \tag{40}$$

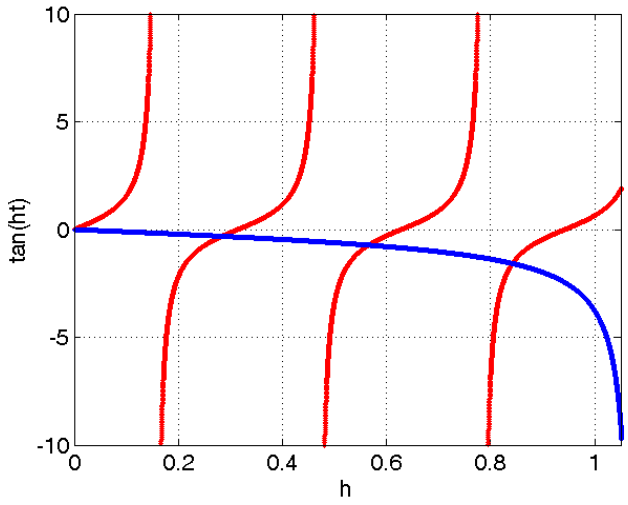

Fig. 5 Eigenvalue equation plotted with the following parameters: $\lambda = 1$ μm, $n_1 = 1.5$, $n_2 = 1$, $n_3 = 1.49$, and $t = 10$ μm.

D. Rib Waveguides

Rectangular rib waveguides are 2-D planar waveguides that have the form as seen below in Fig. 6. This configuration is the same as the chalcogenide rib waveguides used in this research.

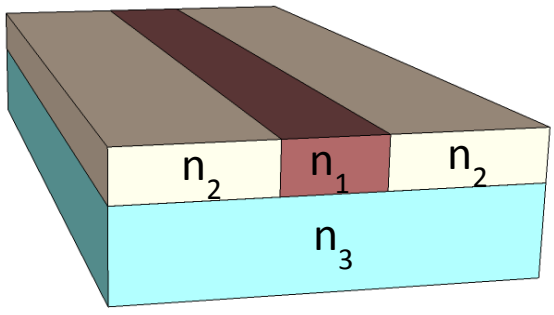

Fig. 6 Rectangular rib waveguide structure.

Because these particular waveguides have this added dimension, there are additional complexities in solving for the modes that are brought about by extra boundary conditions.

Commonly used methods used for solving for the modes are the Marcatili method [12] and the effective index method [13]. Both of these methods break up the waveguide into a 3x3 grid as shown in Fig. 7. The wave guiding core is represented by n_1. The cladding layer is separated into equal segments represented by n_2-n_9 and may be the same depending on the device architecture. The main difference in these two methods is that the Marcatili method ignores regions n_2, n_4, n_7, and n_9, whereas the effective index method takes into account all nine regions.

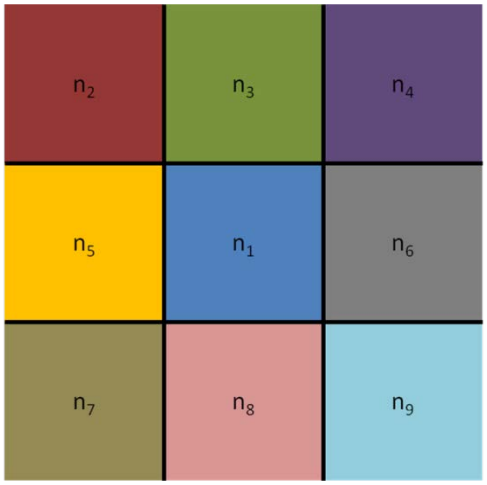

Fig. 7 Grid representation of 2-D rib waveguide.

The Marcatili method works great for well confined modes, but because these outer corner regions are ignored results deviate greatly for modes that are weakly

confined. This method solves the wave equation in each individual region and then adds boundary conditions for the horizontal and vertical directions. Once this is complete, the value for the effective index that satisfies the wave equation for all regions is found.

The effective index method works much better for solving for modes that are weakly confined. This is because all regions are included in the calculations. First, the effective indices for the dimension that limits guiding are found. This is done for each column and leaves a 3x1 grid. The same process is now used on this grid to find the final solutions.

Because these methods are approximate, the FimmWave mode solver package is used to aid in the simulation and design of the devices in this thesis. FimmWave uses mode solving techniques such as the film mode matching (FMM) method and the finite difference mode (FDM) solver. The FMM method is vector based and ideal for rectangular waveguides with small features that can be represented as a finite number of rectangles. The FDM solver is vector based and ideal for high-step refractive index profiles. Various parameters such as refractive index, waveguide dimensions, type of modes to solve for, etc. are entered into the software. FimmWave then solves for the desired number of modes to see each mode's characteristics.

E. Diffused Waveguides

Diffused waveguides are similar to rib waveguides, but instead of having a step-index profile they have a graded-index profile as seen in Fig. 8. This makes it difficult to

identify abrupt boundary positions. As a result of this, the eigenvalue equation becomes an eigen-integral equation [6].

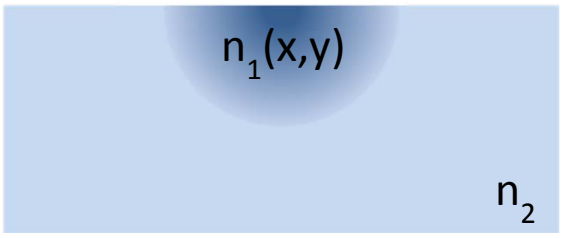

Fig. 8 Diffused waveguide with graded index profile.

For the one dimensional case, the eigen-integral equation is of the form

$$\int_{(x_{t_1})_m}^{(x_{t_2})_m} \sqrt{k_o^2 n^2(x) - \beta_m^2}\, dx = \left(m + \frac{1}{2}\right)\pi \qquad m = 1, 2, 3, \ldots \tag{41}$$

Given that $\beta_m = k_o n_{eff,m}$ and $k_o = 2\pi/\lambda$, (41) becomes

$$\frac{2\pi}{\lambda}\int_{(x_{t_1})_m}^{(x_{t_2})_m} \sqrt{n^2(x) - n_{eff,m}^2}\, dx = \left(m + \frac{1}{2}\right)\pi \qquad m = 1, 2, 3, \ldots \tag{42}$$

where $n_{eff,m}$ is the effective index of the mode m. With the addition of a second dimension, this becomes a double integral which is more complex to solve. Hence, we use commercially available mode solver packages that carry out these calculations rather quickly. Diffused waveguides will be further discussed in Section *C* of Chapter III.

F. Coupling Between Guided Modes

In order to realize devices such as Mach-Zehnder interferometers and ring resonators, coupling must take place between waveguides. Considering the simplest case of two identical waveguides placed in close proximity to one another with a uniform step-index change, as in Fig. 9, one can find the coupled mode equations for waveguides A and B.

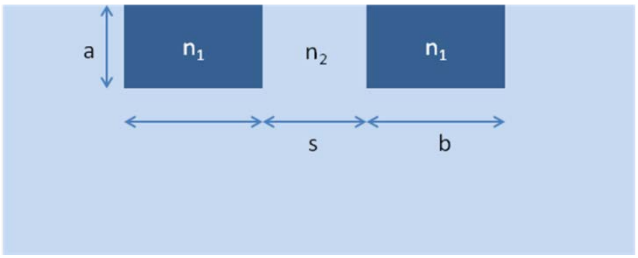

Fig. 9 Two identical parallel waveguides positioned as a directional coupler.

The equations governing the coupling between the waveguides are [6]

$$\left.\begin{aligned}\frac{dA(z)}{dz} &= -j\kappa_{ab}B(z)e^{j(\beta_a-\beta_b)z}\\ \frac{dB(z)}{dz} &= -j\kappa_{ba}A(z)e^{j(\beta_b-\beta_a)z}\end{aligned}\right\} \tag{43}$$

where $\kappa_{ab}=\kappa_{ba}$ is the coupling coefficient. For slab waveguide coupling, κ_{ab} is given by

$$\kappa_{ab}=\frac{2h^2q}{\beta\left(t+\frac{2}{q}\right)\left(h^2+q^2\right)}e^{-qs} \tag{44}$$

where q and h are as defined in (35) and (36), respectively. As can be seen from (44), the coupling depends significantly on the spacing between the waveguides.

While this works great for identical waveguides in close proximity, the use of tapered couplers is needed for waveguides with different cross-sectional dimensions [14] or different refractive indices. To get efficient coupling, the waveguides must be phase matched ($\beta_a = \beta_b$). This is achieved by introducing the second waveguide with a small taper tip and a gradual slope. For our devices, the mode is coupled into an As_2S_3 rib waveguide via a tapered section of As_2S_3.

Recall that κ_{ab} depends on the spacing between the waveguides. Because of this, we would like to put the coupling taper for the rib waveguide directly on top of the diffused waveguide. With Ti:$LiNbO_3$ waveguides, a surface bump is created, which does not allow this to be done without significant losses. APE waveguides have little effect on the surface topology of the substrate; therefore the taper tips of the As_2S_3 rib waveguide are placed directly on top of them. In theory, this should allow for much higher coupling and lower loss from the diffused waveguide to the rib waveguide. The vertical integration of As_2S_3 waveguides is used because of the higher index which allows for a much smaller bending radius than pure Ti:$LiNbO_3$ or APE waveguides. This smaller bending radius leads to the ability to fabricate much smaller devices [15].

CHAPTER III

ANNEALED PROTON EXCHANGE PROCESS

As stated previously, titanium indiffusion and annealed proton-exchange are the two most common methods of forming optical waveguides in lithium niobate. There is great emphasis put in this research on surface smoothness because of the vertical integration of the chalcogenide rib waveguide on top of the APE waveguide. Titanium diffused waveguides (Ti:$LiNbO_3$) must be fabricated at temperatures in excess of 1000°C [16,17] for approximately 10 hours [18]. By comparison, annealed proton exchange waveguides only require an anneal at several hundred degrees, greatly reducing the processing and cool down time [19]. Table II shows a comparison of the time it takes to fabricate Ti:$LiNbO_3$ and APE waveguides. As seen, the APE fabrication process takes less than half the time of Ti:$LiNbO_3$, with the diffusion and proton exchange/anneal steps being the major factors.

Table II
Ti:$LiNbO_3$ and APE Fabrication Time Comparison

Ti:$LiNbO_3$		APE	
Ti Deposition	20 min	SiO_2 Deposition	50 min
Lithography	1 hr	Lithography	1 hr
Etching	30 min	Etching	30 min
Diffusion	11 hr	Proton Exchange	45 min
Cool Down	8 hr	Anneal	2.5 hr
		Cool Down	4 hr
TOTAL TIME	**20.8 hr**	**TOTAL TIME**	**9.6 hr**

Also with Ti:$LiNbO_3$, a thin layer of titanium of approximately 950 Å is sputtered onto the lithium niobate surface [20]. When the titanium is diffused a surface bump approximately twice as thick as the originally deposited titanium layer forms, as is evident from the AFM image shown in Fig. 10 below, whereas with APE waveguides there is an almost immeasurable change in surface roughness.

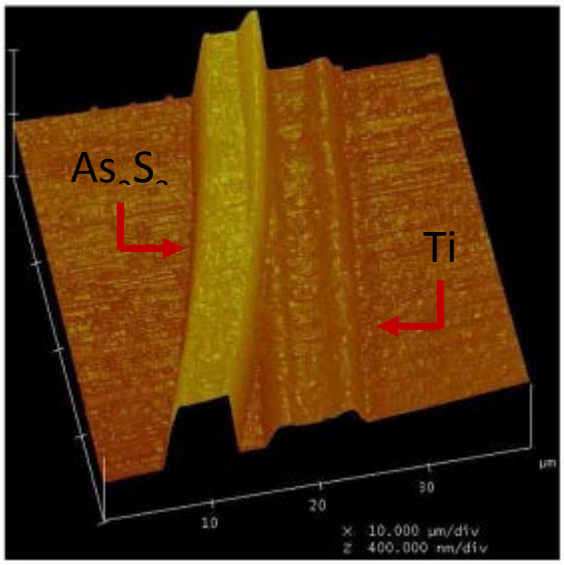

Fig. 10 AFM image of chalcogenide rib waveguide vertically integrated on top of a titanium diffused waveguide [20].

This chapter describes the annealed proton exchange process in detail and explains this method's advantages over titanium diffused waveguides. A detailed background is included along with variations in the proton exchange process. Finally, the modeling of APE waveguides is discussed. These models are extremely important in order to get the right parameters for the fabrication of APE waveguides.

A. Background

Proton exchange is the process of exchanging lithium ions with a proton source such as H^+. A change in the refractive index of the substrate is formed where the exchange takes place. The reaction of the lithium niobate substrate and the hydrogen source is

$$LiNbO_3 + xH^+ \rightarrow Li_{1-x}H_xNbO_3 + xLi^+ \ , \tag{45}$$

which leads to an increase of the extraordinary refractive index n_e [21]. The most common hydrogen source is benzoic acid (C_6H_5COOH), which is a white powder at room temperature. It melts and turns into a liquid at 122°C and begins to boil at 249°C. The first observations of the proton exchange process was by Jackel *et al* [22], in which $LiNbO_3$ was immersed in benzoic acid melts at temperatures of 200-250°C for various lengths of time. This created a step-index guiding layer with an increase in the extraordinary refractive index (Δn_e = 0.12) in x- and z- cut $LiNbO_3$, but damaged y-cut samples. A metal masking layer was used to produce deep strip waveguides ranging from 1-20 μm in width, but these waveguides exhibited high mode-mismatch losses when coupled with optical fibers.

Through research, it has been found that there is a decrease in the ordinary refractive index (Δn_o = -0.04) [23]. Therefore, in x-cut $LiNbO_3$ only the TE mode is allowed to propagate and in z-cut $LiNbO_3$ only the TM mode is allowed to propagate. By use of a prism-coupler method, the ordinary refractive index of proton exchanged waveguides was directly measured. The data obtained was fit and an expression relating the extraordinary and ordinary refractive indices was formulated

$$\Delta n_o = 0.007 - 0.40\Delta n_e \ . \tag{46}$$

In order to get specific wave guiding regions and to prevent full exchange of the substrate surface, a masking layer must be deposited on the surface of the substrate along with subsequent photolithographic steps to open channels. Masking materials commonly used are titanium [24] and silicon dioxide [25]. These materials must be deposited as a high quality thin film in order to prevent exchange in unwanted regions. Once the exchange step is complete and the masking layer has been removed, an almost untouched smooth surface is observed.

In studying the effects of this process, it has been found that proton exchanged lithium niobate suffers from a degradation or reduction of the electro-optic coefficients [26]. Also, because of the continual migration of hydrogen in the exchanged region, instability of the index profile has been observed [27]. These problems can be combated by using diluted melts of benzoic acid with lithium benzoate (C_6H_5COOLi) [28] or with post-fabrication annealing [19]. These two methods effectively reduce the hydrogen concentration in the lithium niobate substrate, which helps with the restoration of the above mentioned critical components. While dilute melt-fabrication allows for these attributes to be restored, it also drastically increases the time needed for fabrication. Post-fabrication annealing also restores these critical attribute, while only increasing fabrication time slightly. For this reason, this work uses the annealed proton exchange technique.

B. Variations in the PE Process

There are many variations in the proton exchange process that have developed. This section will list a few of the variants and briefly describe them. Included are the dilute melt proton exchange process or soft proton exchange (SPE), proton exchange in benzoic acid vapor (PEV), annealed proton exchange (APE), and reverse proton exchange (RPE).

B.1. Soft Proton Exchange

Soft proton exchange is the process by which benzoic acid is diluted into a melt of lithium benzoate or steric acid is diluted into lithium stearate [29]. This allows for the formation of low-loss α-phase waveguides to be formed. When benzoic acid is used by itself, the exchange process forms a β + $HNbO_3$ phase in the substrate [30]. This phase produces unstable waveguides with high fiber-to-waveguide losses. The α-phase waveguides have graded-index profiles and allow for high quality guiding characteristics. More about the phases of $LiNbO_3$ will be discussed in Section *C.3.* of this chapter.

B.2. Proton Exchange in Benzoic Acid Vapor

Proton exchange in benzoic acid vapor is the process by which, instead of immersing $LiNbO_3$ into the benzoic acid melt, the $LiNbO_3$ is exposed to the benzoic acid vapor [31]. This is done by placing the lithium niobate sample into an ampoule's one of two compartments. The other compartment holds the benzoic acid. The ampoule is then

placed into a furnace and allowed to reach thermal equilibrium. Once this point is reached, the sample is exposed to the vapor. This technique allows for the fabrication of high quality low-loss (0.35 dB/cm) α-phase waveguides with a high optical damage threshold.

B.3. Annealed Proton Exchange

Annealed proton exchange is the process by which proton exchanged waveguides are subjected to a post-exchange anneal. This post-exchange anneal is vital in order to produce stable, single mode waveguides. The annealing process takes place at temperatures ranging from 250-500°C for various times [21] and transforms the original step-index proton exchanged waveguide to a gradient-index profile or diffused waveguide [32]. Waveguides fabricated by this method exhibit low propagation loss (0.15 dB/cm), have high coupling efficiency to single-mode fibers (1.2 dB fiber-to-fiber loss), and have no degradation in the electro-optic coefficients [19]. APE is the choice fabrication method for this thesis because of these attributes.

B.4. Reverse Proton Exchange

Reverse proton exchange incorporates the APE method and adds an additional step of submerging the APE sample in a lithium rich mixture. This allows for the formation of buried waveguides [33]. This RPE method allows for better fiber-to-waveguide coupling because of a more symmetric waveguide mode shape, lower losses from a reduction of surface imperfections, and higher conversion efficiency in non-linear

processes due to a better overlap between the interacting modes [34]. This method is not used in this work because of the need for coupling between the As_2S_3 and APE waveguides. As discussed is Section F of Chapter II, coupling depends on the distance between the two waveguides. Therefore, a higher coupling efficiency can be achieved with waveguides fabricated at the surface of the substrate.

C. Modeling Annealed Proton-Exchanged Waveguides

To fabricate annealed proton-exchanged waveguides that meet specific guidelines, accurate simulations and models must be formed to have a better understanding of the characteristics of this process. This section will focus on the modeling of APE waveguides in pure benzoic acid and then focus on simulations for coupling between the APE and As_2S_3 waveguides.

To produce accurate models, the diffusion characteristics of hydrogen from the source into the $LiNbO_3$ substrate must be understood. The exchange depth d_e followed by the anneal depth d_a can be found with existing diffusion equations, which then can be used together to find the total depth $d_t = d_e + d_a$. The total depth of the APE process can then be used to model the hydrogen concentration in the guiding region. This hydrogen concentration model can subsequently be used to find the refractive index profile of the diffused waveguide. These refractive index properties can then be used in software packages such as FimmWave mode solver and FimmProp to simulate and find the mode profiles and characteristics of APE waveguides along with their coupling properties with

As_2S_3 rib waveguides. This research uses x-cut lithium niobate for sample fabrication, therefore all simulations and numbers are for this particular substrate cut.

C.1. Exchange Depth Model

As stated earlier, the proton exchange process produces a step-index waveguide with width w and depth d_e which is shown in Fig. 11. If there is no change in the hydrogen concentration from the benzoic acid source, the exchange process is only dependent on time and temperature [35].

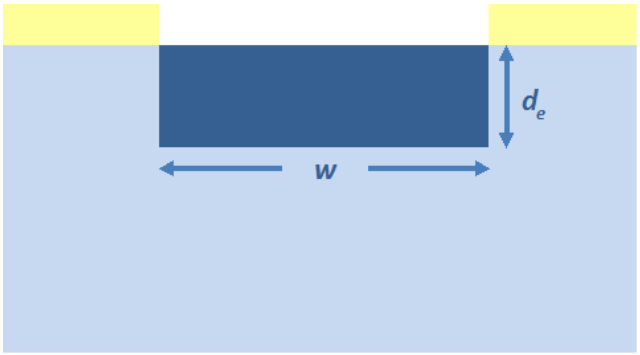

Fig. 11 Proton exchange depth model with width w and exchange depth d_e.

The exchange depth d_e is represented by

$$d_e = 2\sqrt{tD_e(T)} \tag{47}$$

where t is the time of the exchange in hours and $D_e(T)$ [μm^2/hr] is dependent on temperature and expressed by the Arrhenius equation

$$D_e(T) = D_e^o e^{\left(\frac{-Q}{R_o T}\right)}. \quad (48)$$

D_e^o is the diffusion constant for the exchange, Q is the activation energy of the process, R_o = 8.3144621 [J/(mol*K)] is the Boltzmann constant, and T is the exchange temperature. Different values of the diffusion constant and activation energy from literature can be found in Table III. By comparing fabricated work with simulations through various trials with the constants given in literature, the activation energy used by Loni of Q = 79.3 eV/mol and a diffusion constant of D_e^o = 0.7725x10^8 μm^2/h, which is in the range of published diffusion constants, was found to best model the setup conditions in our lab.

Table III
Diffusion Constants and Activation Energies

	Wong [35]	de Almeida [36]	Loni [37]
D_e^o [10^8 μm^2/h]	4.326	0.48	1.5
Q [eV/mol]	84	77.4	79.3

This information was used to plot the diffusion coefficient for various temperatures. Once this was complete, the diffusion coefficient for the temperature of 200°C was found and used to plot the exchange depth versus time. As can be seen in Fig. 12, this process is highly dependent on time which must be kept constant throughout the process for desirable results.

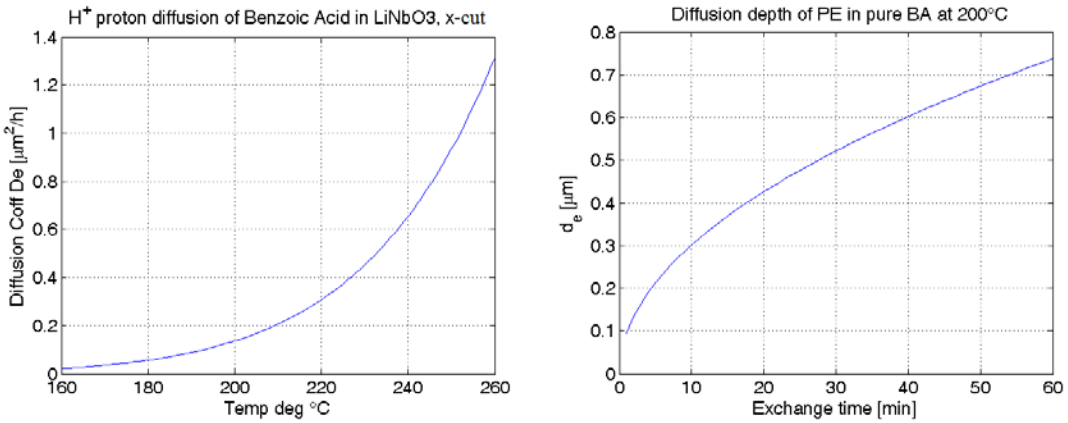

(a) (b)

Fig. 12 Diffusion coefficient and exchange depth plots. a) Diffusion coefficient plotted for a temperature range from 160-260C. b) Diffusion depth of the xchange process plotted versus time.

C.2. Anneal Depth Model

The anneal depth model uses the same diffusion principles as the exchange depth model, but because the thermal anneal changes the waveguide from step-index to a graded-index structure, the model given in Fig. 8 is used. This anneal step further drives the hydrogen into the substrate causing the H^+ to have a less dense concentration farther from the surface. As with the exchange depth, the anneal depth d_a is a function of temperature and time. The anneal depth is therefore expressed by [30]

$$d_a = 2\sqrt{tD_a(T)} \tag{49}$$

where t is the time of the anneal in hours and $D_a(T)$ [μm^2/hr] is the temperature dependent Arrhenius equation representing the anneal diffusion coefficient expressed by

$$D_a(T) = D_a^o e^{\left(\frac{-H}{R_o T}\right)} \tag{50}$$

where D_a^o is the diffusion constant for the anneal, H is the activation energy, R_o is the Boltzmann constant, and T is the exchange temperature. Because this diffusion occurs in both the vertical and horizontal directions the values for z-cut $LiNbO_3$ are needed. Table IV displays the anneal diffusion constants and activation energies from literature with the values from de Almeida used for this research. Fig. 13 displays the anneal depth versus time for the values presented by de Almeida for an anneal temperature of 400°C.

Table IV
Anneal Diffusion Constants and Activation Energies for X- and Z-Cut $LiNbO_3$

	de Almeida [36]		Howerton [30]		Zavada [38]	
	x-cut	z-cut	x-cut	z-cut	x-cut	z-cut
D_a^o [10^{12} μm^2/h]	22	0.4	0.27	-	-	0.01
H [eV]	1.77	1.5	1.44	-	-	1.21

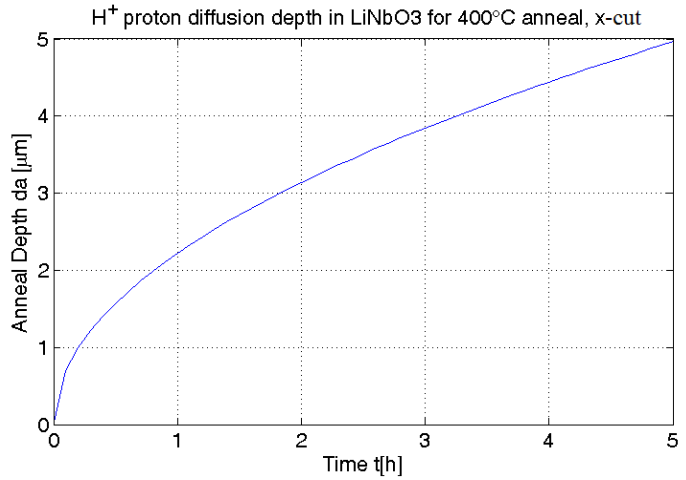

Fig. 13 Anneal diffusion depth for times from 1-5 hours at 400°C.

C.3. Bidimensional Hydrogen Concentration Model

The exchange reaction as noted in (45) is represented by a fractional hydrogen concentration *x*. The $LiNbO_3$ crystal phase is determined by the value of this fractional hydrogen concentration and is represented in Table V [30]. The initial proton exchanged substrate are in the β + $HNbO_3$ phase and transition to the low-loss alpha phase during the anneal process. With this being said, it was found that $d_a/d_e \geq 7.5$ for the α phase to be achieved.

Table V
$LiNbO_3$ Crystal Phases Associated With Their Fractional H^+ Concetration

Phase	**Fractional H^+ Concentration**
α	$x \leq 0.12$
α + β	$0.12 \leq x \leq 0.56$
β	$0.56 \leq x \leq 0.75$
β + $HNbO_3$	$x \geq 0.75$

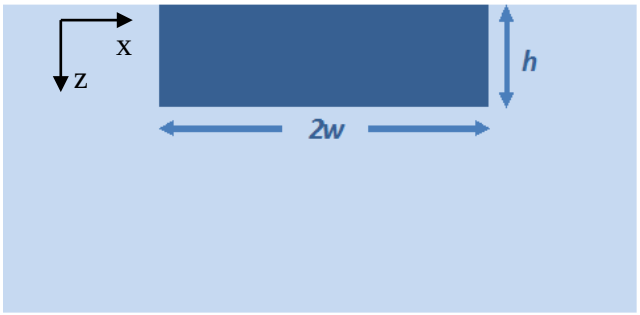

Fig. 14 Model for bidimension hydrogen concentration with its diffusion directions.

The bidimensional hydrogen concentration is dependent upon depth and width, therefore the model parameters seen in Fig. 14 are used. Because the anneal diffusion happens both vertically and horizontally, the hydrogen concentration must be modeled in both the x and z directions. Therefore, the concentration profile is given by [36]

$$C_H\left(x,z,t_a\right)=\frac{C_o}{4}\left[erf\left(\frac{h+z}{d_v}\right)+erf\left(\frac{h-z}{d_v}\right)\right]\left[erf\left(\frac{w+x}{d_h}\right)+erf\left(\frac{w+x}{d_h}\right)\right] \quad (51)$$

where $d_v = d_e + d_a$ is the diffusion in the z direction and $h = d_e$ is the initial exchange depth. Here the vertical diffusion depth d_v and the horizontal diffusion depth d_h are represented the same as (47) and (49). With this being established the index profile can be found by

$$\Delta n_e\left(z,t_a\right)=\frac{\Delta N_{pp}}{2}\left[erf\left(\frac{d_e+z}{d_a}\right)+erf\left(\frac{d_e-z}{d_a}\right)\right] \quad (52)$$

where ΔN_{pp} is the peak index change at the surface of the substrate.

Using all the above data, including the exchange and anneal depths models were formed to find the index distribution for certain parameters as seen in Fig. 15. The values used were: an exchange temperature of 200°C, exchange time of 15 minutes, anneal temperature of 400°C, and anneal time of 2.5 hours. These parameters yielded the values listed in Table VI .

Table VI
Values Obtained from APE Waveguide Modeling

Parameter	Obtained Value
d_e	0.369 µm
d_v	3.879 µm
d_h	5.0889 µm
Δn_e	0.00988
d_a/d_e	9.519

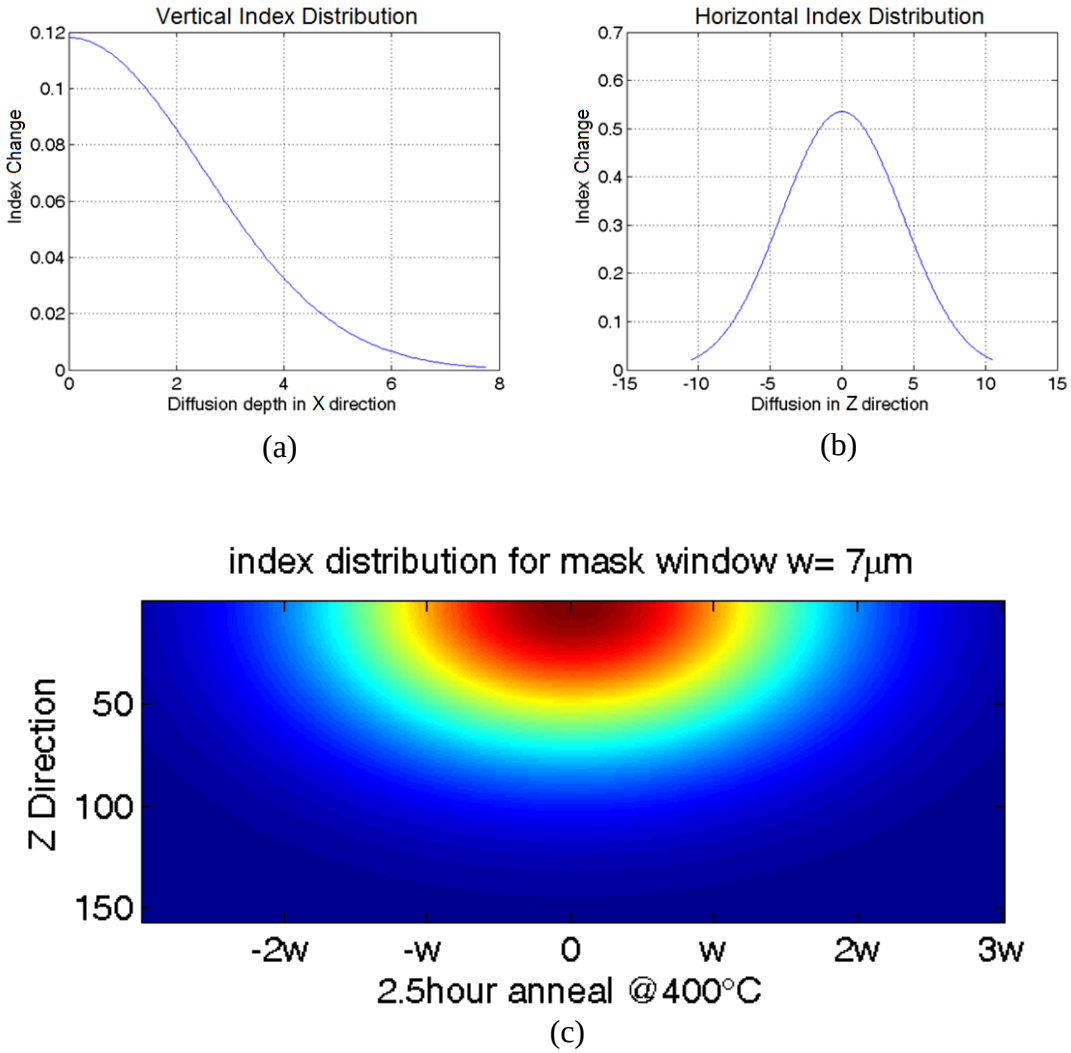

Fig. 15 Modeled index profile for a width of 7 µm, exchange temperature of 200°C for 15 minutes, and anneal temperature of 400°C for 2.5 hours. a) Index distribution in the x direction. b) Index distribution in the z direction. c) Index distribution in the vertical and horizontal directions.

C.4. Mode Profile Simulations

The obtained values were entered into FimmWave to simulate the wave guiding structure. This provided the ability to see if the waveguides were single mode or multi-mode, find their effective area, and calculate their mode field diameter (MFD), amongst other characteristics. The mode profiles were then plotted from the data obtained from FimmWave and are given in Fig. 16.

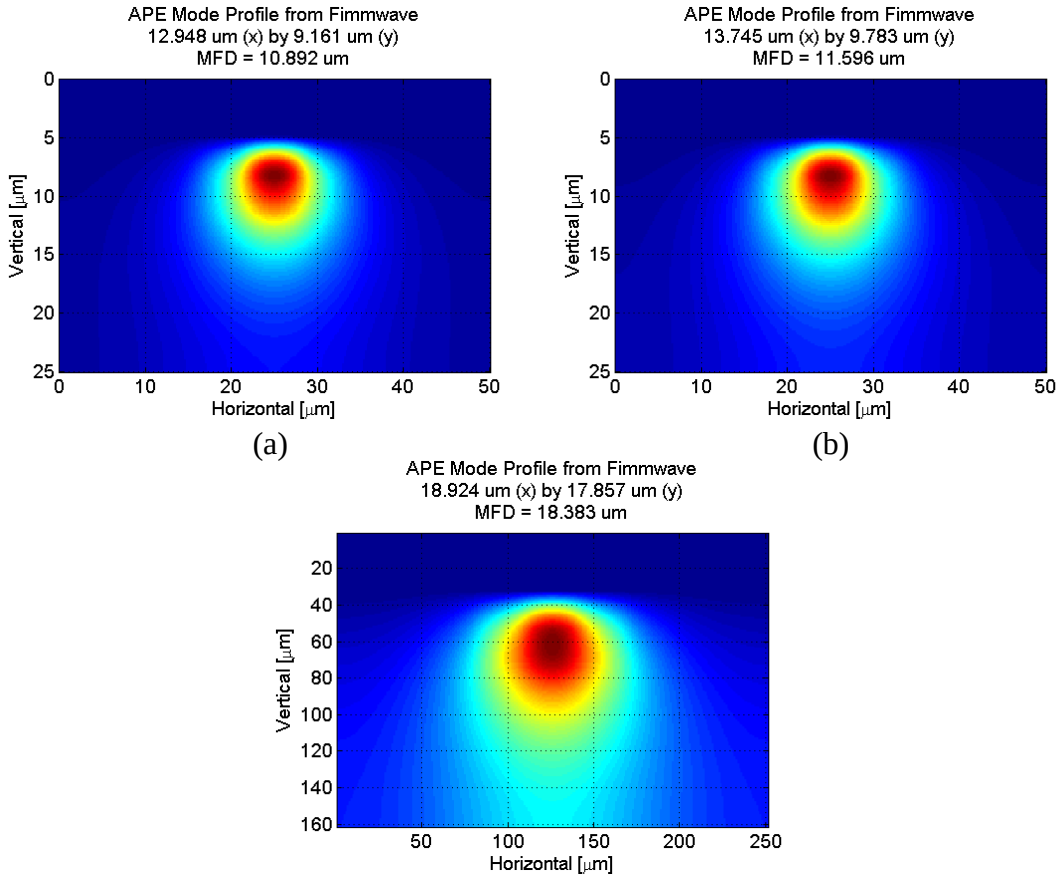

Fig. 16 Simulated Mode Field Diameter. All have an exchange time of 15 minutes, exchange temperature of 200°C, and exchange temperature of 400°C. a) Mode Profile with exchange time of 2.5 hours. b) Mode Profile with exchange time of 3 hours. c) Mode Profile with exchange time of 4 hours.

It can be seen that the longer anneal time causes the mode field diameter to become larger with a great difference between 3 and 4 hours. The coupling efficiency η, or the mismatch factor, can be calculated for our simulated waveguide and a single mode fiber with MFD = 10.7 μm by [39]

$$\eta = 2\frac{\left[\left(\frac{1}{a^2}+\frac{1}{\sigma_1^2}\right)^{-1/2}+\left(\frac{1}{a^2}+\frac{1}{\sigma_2^2}\right)^{-1/2}\right]^2}{a^2\sigma_3\left(\sigma_1+\sigma_2\right)\left[\frac{1}{a^2}+\frac{1}{\sigma_3^2}\right]} \tag{53}$$

where *a* is the half width of a single mode fiber, σ_1 and σ_2 are the half widths of the vertical asymmetric Gaussian profile of the waveguide mode, and σ_3 is the half width of the horizontal symmetric Gaussian profile of the waveguide mode. The mismatch loss can then be found by

$$mismatch\ loss = -10\log\left(\eta\right)\ . \tag{54}$$

C.5. Mode Coupling Simulations

Coupling simulations were then performed with the simulated APE waveguide from above with parameters given in Table VI. An As_2S_3 rib waveguide was side coupled and vertically coupled to the simulated APE waveguide and modeled with taper width of 1.0-1.9 μm, taper length of 2000 μm, and As_2S_3 thickness of 2800 Å. The progression from the taper tip of 1.0 μm to the end of the taper can be seen in Fig. 17 for side coupling and Fig. 18 for vertical coupling. The side coupling showed ~94.8% coupling and ~4.5% scattering losses, whereas the vertical coupling showed ~99.1%

coupling with ~0% scattering losses. Therefore the use of vertically integrated chalcogenide rib waveguides is preferred for higher coupling.

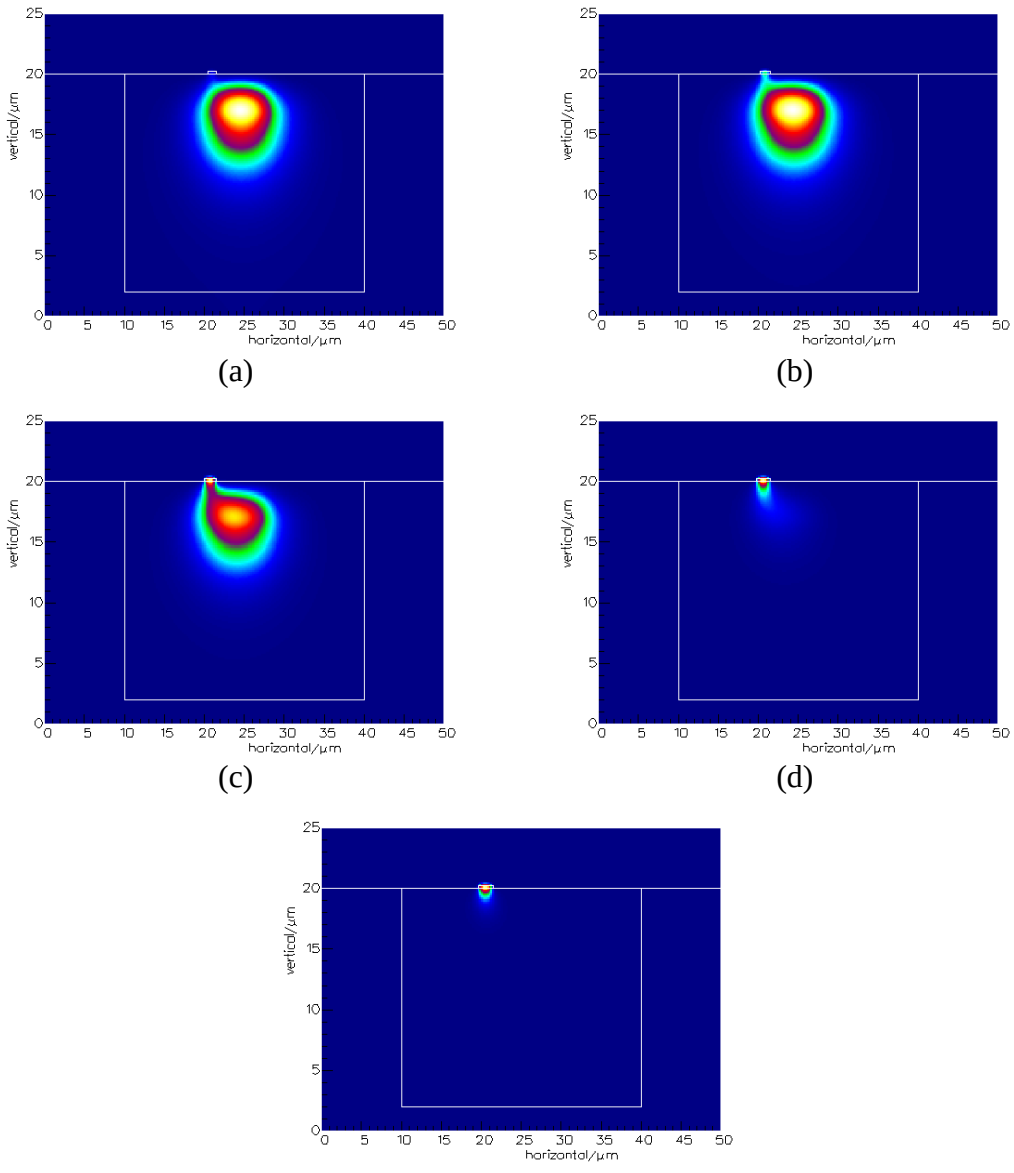

Fig. 17 Side coupling progression from APE waveguide to As_2S_3 rib waveguide. a) 1.0 µm width at taper tip. b) 500 µm distance. c) 1000 µm distance. d) 1500 µm distance. e) 1.9 µm width at 2000 µm distance.

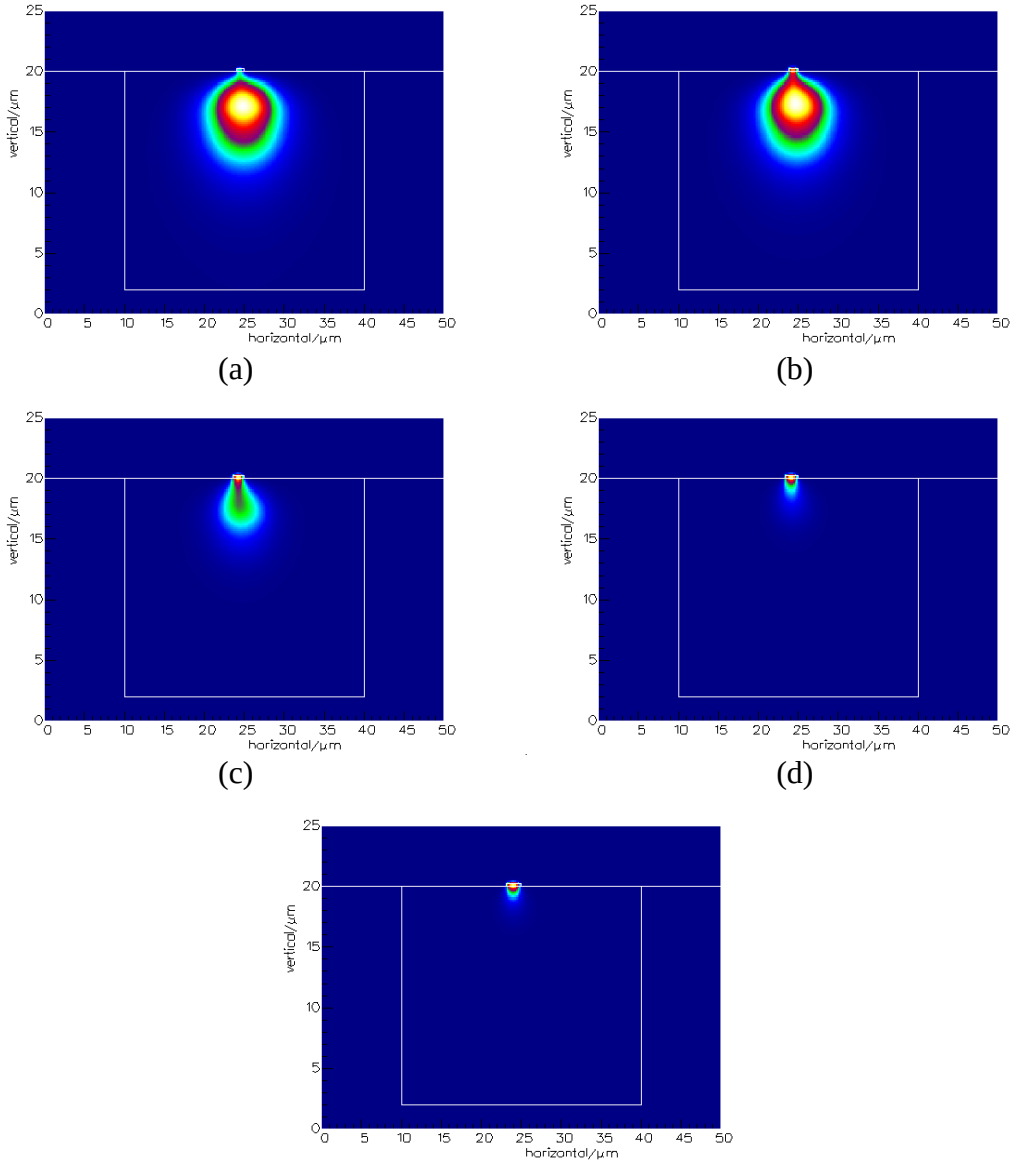

Fig. 18 Vertical coupling progression from APE waveguide to As_2S_3 rib waveguide. a) 1.0 μm width at taper tip. b) 500 μm distance. c) 1000 μm distance. d) 1500 μm distance. e) 1.9 μm width at 2000 μm distance.

CHAPTER IV

DEVICE FABRICATION

This chapter focuses on the fabrication of annealed proton-exchanged waveguides, along with the vertical integration of chalcogenide rib waveguides. Each step in the process will be examined and explained thoroughly. The steps of the proton exchange process are visualized below in Fig. 19.

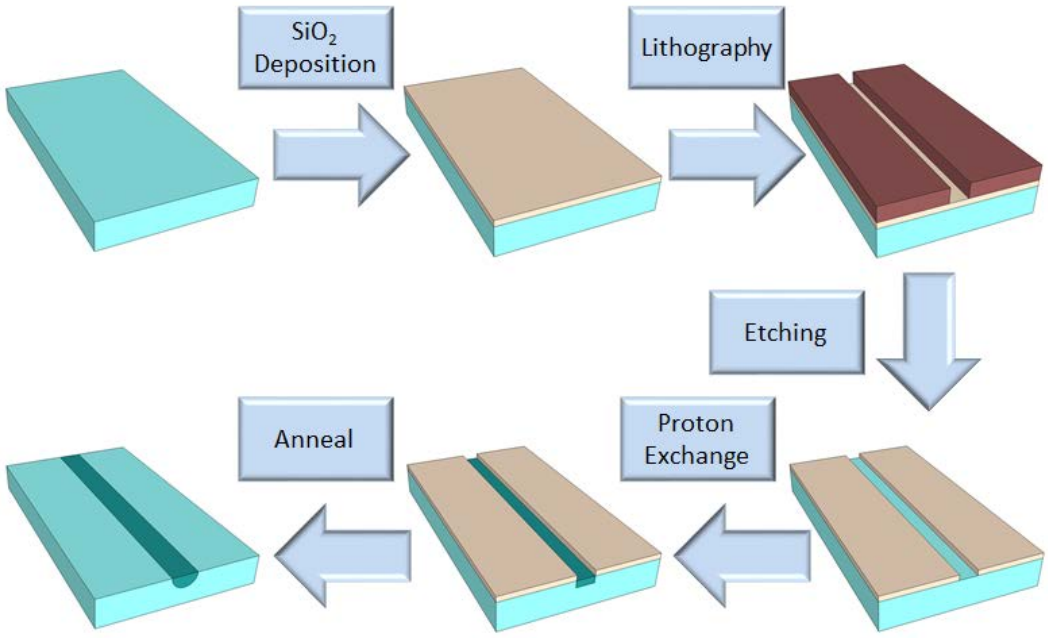

Fig. 19 Fabrication Process flow for APE waveguides.

A. Sample Preparation

Lithium niobate from Crystal Technology, LLC arrives in 3 inch wafers 1 mm in thickness. These are x-cut y-propagating, so that after the proton exchange process is complete the TE mode is only allowed to propagate. In order to fabricate waveguide devices on this substrate, it needs to be diced and thoroughly cleaned. A MicroAutomation 1100 Wafer Dicing Saw is used to make 20 x 22 mm samples as seen in Fig. 20. Once diced, the samples must be cleaned with extreme care in order to prevent residual particles from contaminating the deposition phase. First, the $LiNbO_3$ sample is cleaned with soapy water and a q-tip. After that, acetone, methanol, and isopropanol (IPA) are used, in that respective order, to further clean the substrate and to prevent spotting. Nitrogen gas is used to dry samples.

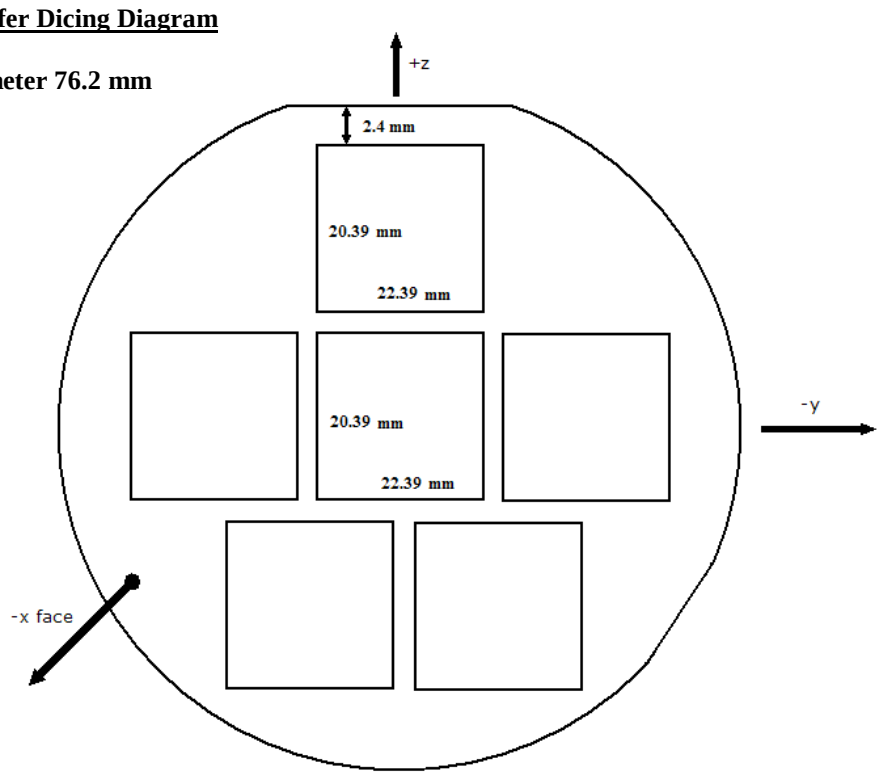

Fig. 20 Dicing diagram for $LiNbO_3$ wafer.

B. Deposition

Now that the samples are prepared, they are ready for the masking layer. This masking layer will help prevent proton exchange from occurring in unwanted regions, therefore, surface uniformity and quality are vital. Silicon dioxide (SiO_2) is the chosen material. The deposition is carried out by an AJA DC/RF Magnetron Sputtering system by which recipes were developed to adhere to the key requirements stated above. Argon and Oxygen are flowed at 40 sccm and 1.5 sccm, respectively. The sputtering system is operated at 3 mT with an RF power of 200 W. A thin film of 1000-2000 Å is sputtered onto the surface of the $LiNbO_3$ substrate.

C. Photolithography

Photolithography is simply the transfer of an image or pattern to the surface of a substrate by exposing it to light. To get this pattern, a photolithography mask is needed. The mask is designed on specialized software, such as OptiBPM or L-Edit, and is transferred to a quartz plate where the pattern is formed with chrome. Because an opened channel is needed and positive lithography is employed, an image reversed mask is designed and can be seen in Fig. 21.

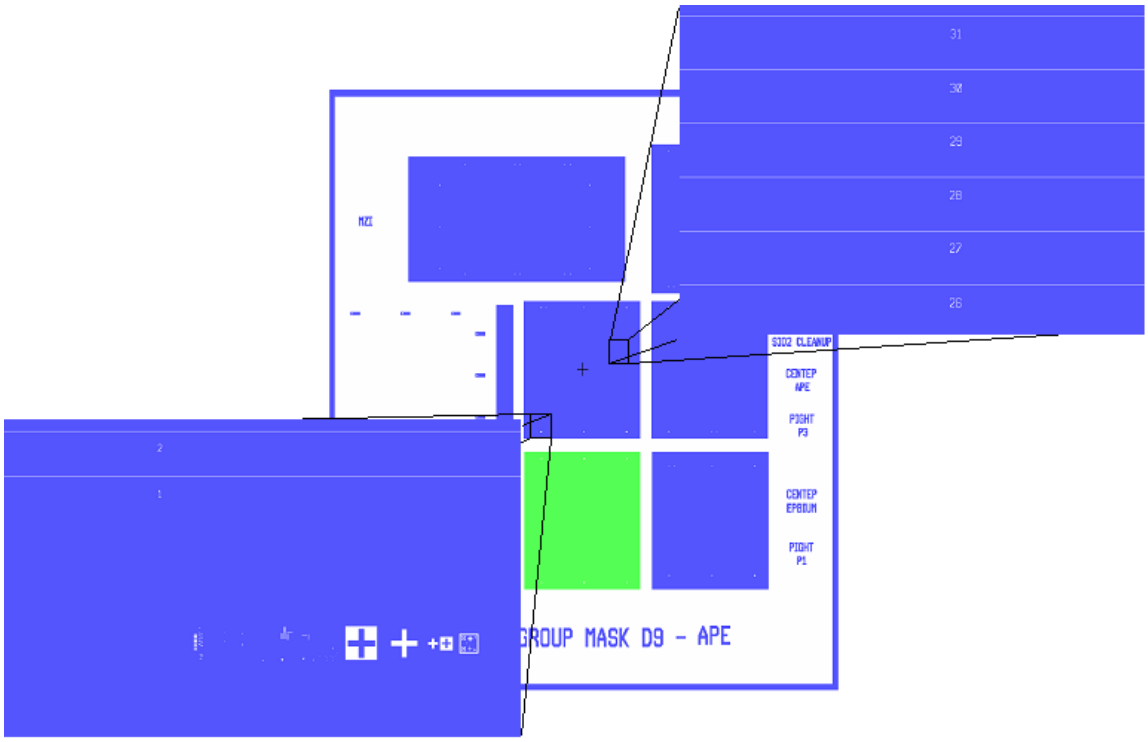

Fig. 21 Image reversed photolithographic mask for APE. Top projection – straight waveguides for APE fabrication. Bottom projection – alignment marks for chalcogenide vertical integration.

After deposition, the sample is, again, cleaned with acetone, methanol, and isopropanol to prevent particles from transferring to the patterned film. A thin layer of AZ5214 positive photoresist is spin coated onto the sample at 4000 RPM for 50 seconds. Once that is complete, a soft bake step takes place on a hotplate at 125°C for 1 minute. The setup used is a Karl Suss MA6 contact mask aligner that operates at the peak ultraviolet spectrum of 365 nm, or also known as an i-line exposure aligner. An intensity reading is carried out on the UV light to find the exposure time for the desired dosage. Dosage and exposure time are a critical part of this process. If one or the other is wrong, the sample can become over or under developed as pictured in Fig. 22. The mask is placed on the MA6 along with the photoresist prepared sample and they are subsequently aligned, then exposed.

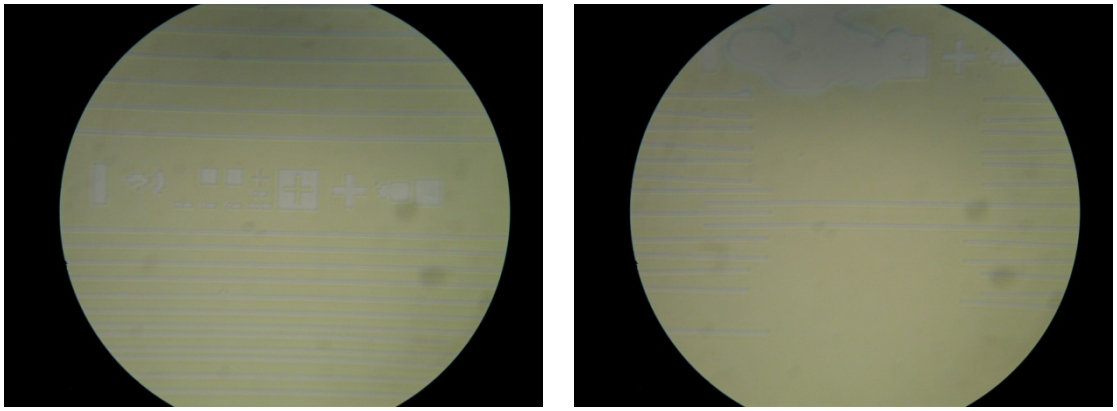

(a) (b)

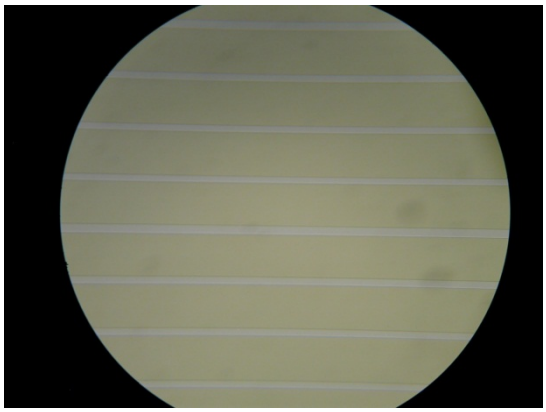

(c)

Fig. 22 AZ5214 photoresist after development. a) Underdevelopment of photoresist (70 mJ/cm^2). b) Overdevelopment of photoresist (95 mJ/cm^2). c) Good Development (85 mJ/cm^2).

Once the exposure is complete, the sample is developed in a mixture of MF312 photoresist developer and DI-water in a ratio of 6 parts DI-water to 5 parts MF312. It has been found that an exposure dosage of 85 mJ/cm^2 and development time of approximately 55 seconds is ideal for this lab setting, as alluded to in Fig. 22. After that is complete, the sample is hard baked in a dehydration oven at 135°C for 8 minutes.

D. Etching

Now that the mask pattern is transferred, openings must be made in the SiO_2 mask layer so as to expose the lithium niobate surface. This is done by either an isotropic wet etch or an anisotropic dry etch.

D.1. Wet etching

Wet etching involves immersing the sample into a chemical etchant, such as hydrofluoric acid (HF). This is an isotropic process, which means it etches in both the vertical and horizontal directions as shown in Fig. 23. Although this will allow for the surface of the substrate to be, effectively, untouched, this isotropic etch poses a problem. This is because over etching will cause the channel opening to become wider than anticipated, which will in turn alter the entire APE process.

Fig. 23 Isotropic wet etch.

D.2. Dry etching

The dry etching process is more favorable for the use of opening channels of specific width because it only etches in the vertical direction as seen in Fig. 24. Although the dry etching process is more complicated and over etching is still a problem because it can slightly degrade the surface of the substrate, it offers a much higher selectivity than wet etching. Reactive Ion Etching (RIE) is chosen for this research and is operated at a pressure of 10 mT with RF and ICP powers set to 100 W and 200 W, respectively. The substrate temperature is held at 15°C while 25 sccm of CHF_3 and 5 sccm of Ar are flowed into the system. Etching of the SiO_2 masking layer is approximately 60 nm/min. After etching is complete, the photoresist is removed with AZ300T photoresist stripper.

Fig. 24 Anisotropic dry etch.

E. Proton Exchange

Proton exchange is realized by submerging the lithium niobate sample into a benzoic acid melt. Benzoic acid is a powdered solid at room temperature and must be heated to at least 122°C to melt, with the desired exchange temperature being 200°C. PE

is an extremely temperature dependent process, so it is vital that the temperature remain stable throughout the process. Others have used sealed ampoules [31] and heated silicone oil baths [36] in order to get desired results. In this research, the setup consists of an insulated beaker, hotplate, magnetic stirrer, and thermal probe, as pictured in Fig. 25. The insulation is removable and is made of a fiber glass mesh with a polytetrafluoroethylene (PTFE) lid that has a melting point of 327°C. These materials were chosen because of their high temperature tolerance. Attached to the lid, is a sample holder where the sample is placed.

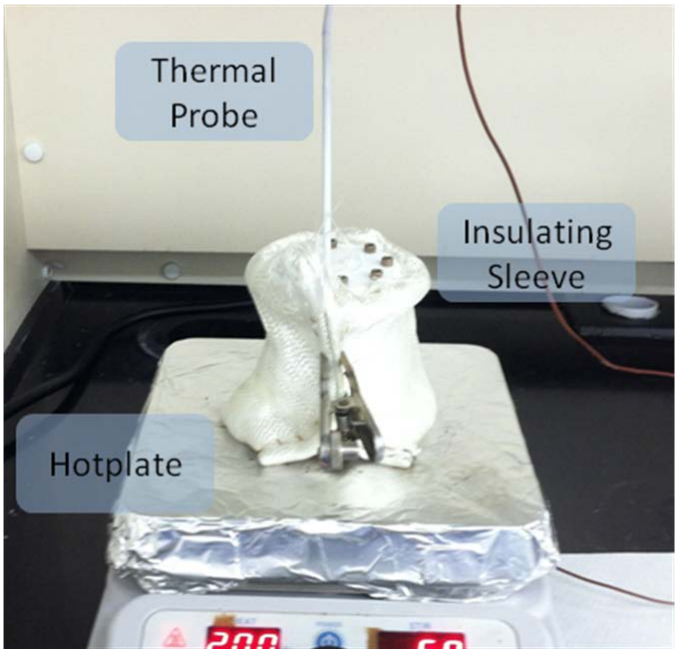

Fig. 25 Proton Exchange setup consisting of an insulated beaker, hotplate, and thermal probe.

The 100 mL beaker used in this setup is filled with 60-80 mL of benzoic acid and allowed to reach the desired operating temperature of 200°C before the sample is submerged. When the acid reaches the exchange temperature (approximately 20 minutes), a magnetic stirrer is placed in the bottom of the beaker for further temperature consistencies. Extreme caution is taken when lowering the $LiNbO_3$ sample into the melt as to avoid thermal shock and cracking the sample. This process consists of holding the sample, which is on the sample holder, above the acid for 1-2 minutes to reach thermal equilibrium, then slowly lowering it into the acid. The sample is submerged and exchanges for 15-30 minutes.

After the exchange is complete, the sample is slowly raised from the benzoic acid, with the same care as before, to again avoid thermal shock. The lithium niobate sample is allowed to cool, then is soaked in isopropanol for a few minutes to remove the excess benzoic acid. If needed the sample is cleaned gently with a q-tip soaked in IPA.

F. Annealing

As discussed in Chapter 3, “as-is” proton exchanged waveguides are unstable and suffer from degradation of the electro-optic coefficients. Additional losses are brought about by fiber-to-waveguide coupling. PE waveguides have a step index profile, whereas a single mode fiber (SMF) has a symmetric Gaussian distribution, which causes mode mismatch losses. To combat and restore these properties, an anneal step is employed by use of a diffusion furnace.

Fig. 26 Diffusion furnace used for the annealing of proton exchanged waveguides.

The diffusion furnace consists of an insulated glass tube surrounded by heating coils, as pictured in Fig. 26. Typical annealing temperatures for proton exchanged waveguides, as discussed earlier, range from 250-500°C. The furnace is allowed to reach the temperature of 400°C, which is the temperature utilized in this study. This temperature is much less than that of titanium diffused waveguides, which uses temperatures in excess of 1000°C. A ceramic sample holder, or “boat”, is used to hold the PE $LiNbO_3$ sample and is placed in the center of the diffusion furnace as to avoid temperature gradients. Wet breathing air is flowed through the furnace at 30 sccm to aid in the process. The anneal process is carried out for 1-4.5 hours and results in a graded index diffused waveguide.

G. Polishing

In order for fiber-to-waveguide losses to be minimized, the ends of the APE $LiNbO_3$ samples must be polished. The edges are extremely jagged and rough due to the initial dicing procedure. The polishing setup consists of a Struers MD Diamond Grit Polishing machine with a magnetic rotary used to hold the polishing pads, a water spout used to drip DI-water onto the polishing pad to remove residual $LiNbO_3$ from damaging sample edges, and a speed controller used to adjust the speed of rotation of the rotary, as seen in Fig. 27.

Fig. 27 Polishing setup consisting of polishing pad rotary, water spout, and speed controller.

Diamond grit polishing pads of different grain size are used to incrementally smooth the edges of the sample. The waveguides may not initially reach the edge of the sample, so the edge must be polished down in order for light to be able to couple.

The first diamond grit polishing pad used has a grain size of 15 μm and is rotated at a speed of approximately 135 RPM. This procedure is carried out for 2 minute or until the waveguides reach the edge of the substrate. This is checked under a microscope and is pictured in Fig. 28.

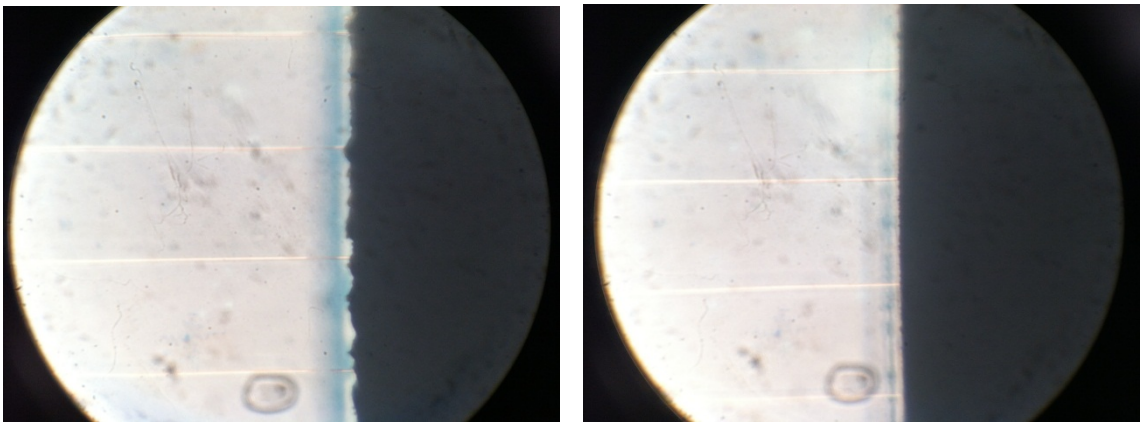

(a) (b)

Fig. 28 Examination of sample. a) Before 15 μm polishing pad is used. Waveguides do not reach edge of sample b) After 2 minutes of 15 μm polishing pad usage.

After the polishing allows the waveguides to reach the edge, a 3 μm diamond grit polishing pad is used. The pad is rotated at approximately 85 RPM for 2 minutes or until desirable results are achieved. The sample is again checked under microscope throughout the process, with the face of the edge examined at this time.

The final polishing pad used is a super-fine grit 0.5 μm grain sized diamond grit pad. It is rotated at approximately 55 RPM for 2 minutes or, again, until the desired results are achieved. The results of these steps can be seen in Fig. 29 below. Table VII includes detailed steps of the fabrication process and its timeline.

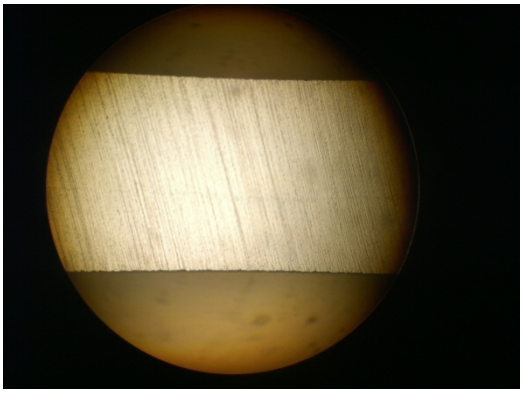

(a)

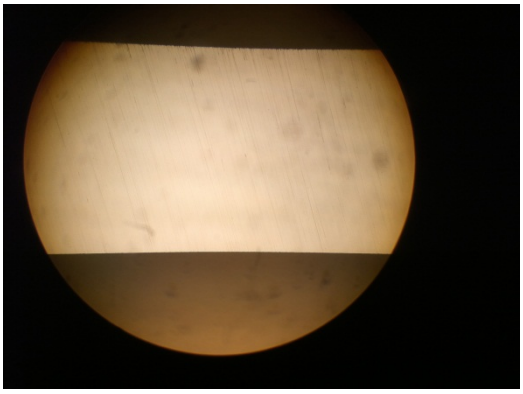

(b)

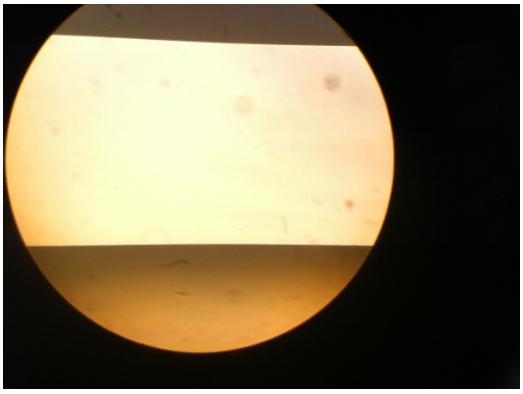

(c)

Fig. 29 Examination of polished edges. a) Edge face after use of 15 µm pad. b) Edge of face after use 3 µm pad. c) Edge of face after use of 0.5 µm pad.

Table VII
Detailed fabrication process and time table.

Process	Details	Time
SiO_2 Deposition	RF Magnetron Sputter	~50 min
Lithography	Spin on Resist, soft bake, expose, develop, hard bake	~1 hr
Etching	Reactive Ion etch (~60nm/sec)	~30 min
Resist Strip	AZ300T and cleaning	~1 hr
Proton Exchange	Benzoic acid bath and cleaning	~45 min
Anneal	Tube furnace (additional time needed for furnace cooling)	~2.5 hr
Polishing	Struers MD Diamond Grit Polishing	~1hr 30min

H. MZI Fabrication

The fabrication of the Mach-Zehnder Interferometer (MZI) is similar to the above explained procedures, so only the differences will be explained in this section. This section will focus on the fabrication of arsenic trisulfide (As_2S_3) chalcogenide rib waveguides, Fig. 30. Once the polishing of the APE waveguides is complete, the SiO_2 masking layer is removed by wet etching with a diluted (1:30) HF:DI-Water mixture.

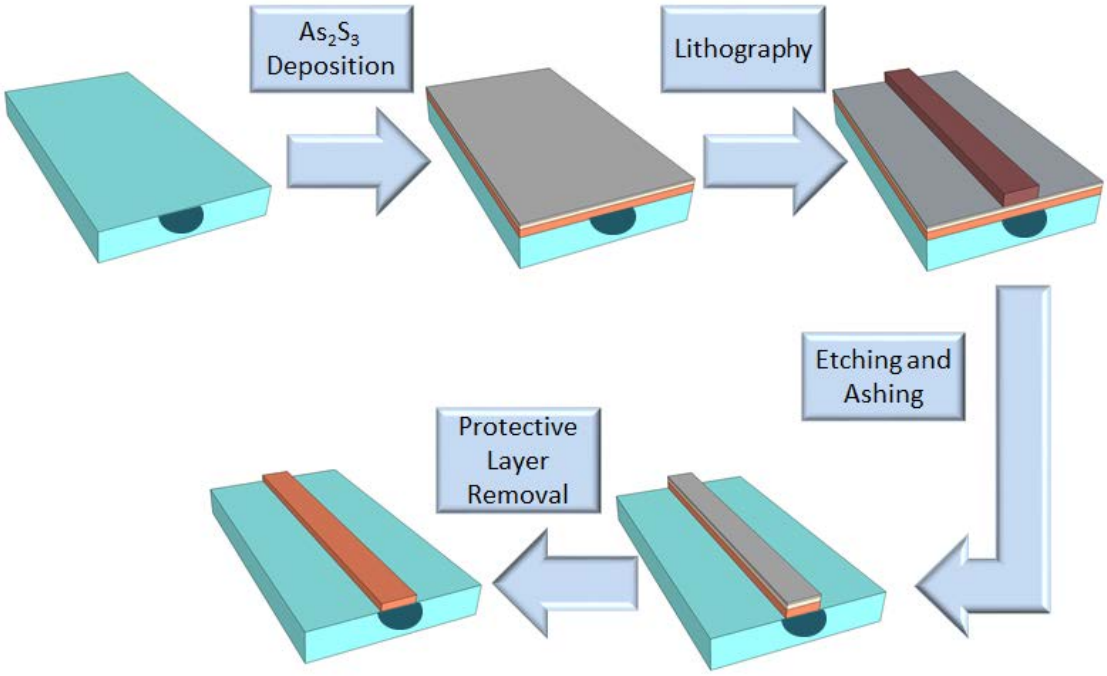

Fig. 30 Fabrication process flow of As_2S_3 waveguides.

H.1. As_2S_3/Protective Layer Deposition

Deposition of the As_2S_3 is accomplished with the same sputter machine as mentioned earlier. Also, a SiO_2/Ti protective layer is sputtered on top of the As_2S_3. This

protective layer is needed because the chalcogenide reacts with the MF312 photoresist developer, which acts as an etchant.

H.2. As_2S_3 Photolithography

In the photolithography process, the resist is spun on at 7000 RPM for 50 seconds, soft baked at 125°C for 1 minute, exposed with 85 mJ/cm^2 dosage, developed for approximately 55 seconds, and hard baked for 30 minutes.

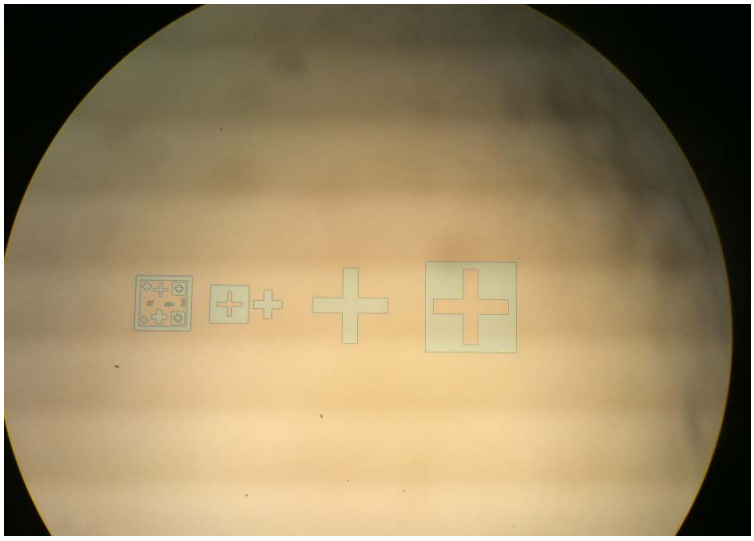

Fig. 31 Alignment marks fabricated during the APE process to use for alignment of the chalcogenide high resolution mask.

The photolithography step of the chalcogenide involves aligning the designed As_2S_3 MZI high resolution mask with alignment marks, as seen in Fig. 31, which have been fabricated in the initial lithography step, Fig. 32. This is so that the rib waveguides

are fabricated in the required spot for vertically coupling the light from the APE waveguide to the chalcogenide waveguide.

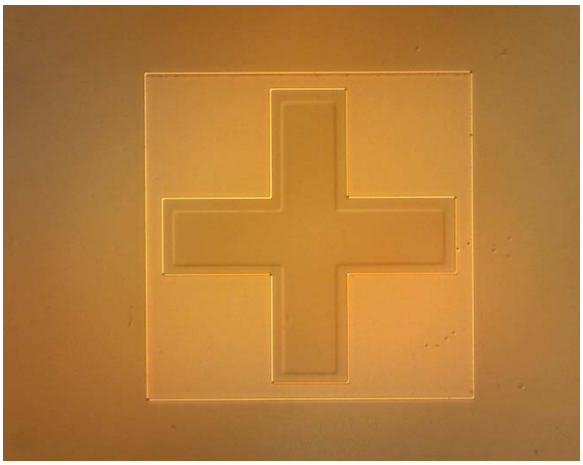

Fig. 32 As_2S_3 alignment mark aligned with APE alignment mark.

H.3. As_2S_3 Etching

Etching is done by RIE with the same parameters as above. An extra O_2 ashing step is included after etching to remove the photoresist. This is because As_2S_3 also reacts with the AZ300T photoresist stripper. The O_2 ashing parameters include 100 sccm of O_2, a pressure of 40 mT, substrate temperature of 25°C, with 100 W RF power, and no ICP.

CHAPTER V

MEASUREMENTS & RESULTS

The transmission spectrum of the fabricated APE waveguides is found using the LUNA Optical Spectrum Analyzer, which sweeps through a range of telecommunications wavelengths from 1525-1610 nm. Before the chalcogenide is deposited onto the surface of the APE waveguide device, optical transmission measurements are taken to ensure low-loss single mode waveguides. The optical fiber from the LUNA is butt coupled with the APE waveguide and index matching gel is used to reduce reflections between the optical fiber (n = 1.45) and the APE waveguide (n ≈ 2.3), Fig. 33.

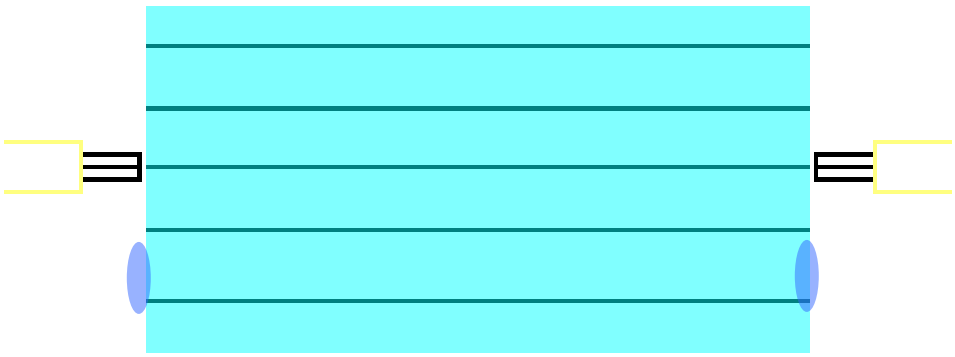

Fig. 33 Optical fibers butt coupled to APE waveguides with the aid of index matching gel.

A. APE Waveguide Measurements

Translation stages are used to aid in the alignment of the fibers and waveguide. Miniscule adjustments are made in order to get the best results, i.e. lowest losses, possible. The data from these measurement results was read into MATLAB and plotted so that the transmission results could be visualized. Beam profile measurements were also taken of all the fabricated devices. These results can be observed in the next section and compared to the LUNA measurement results.

A.1. Initial APE Fabrication Results

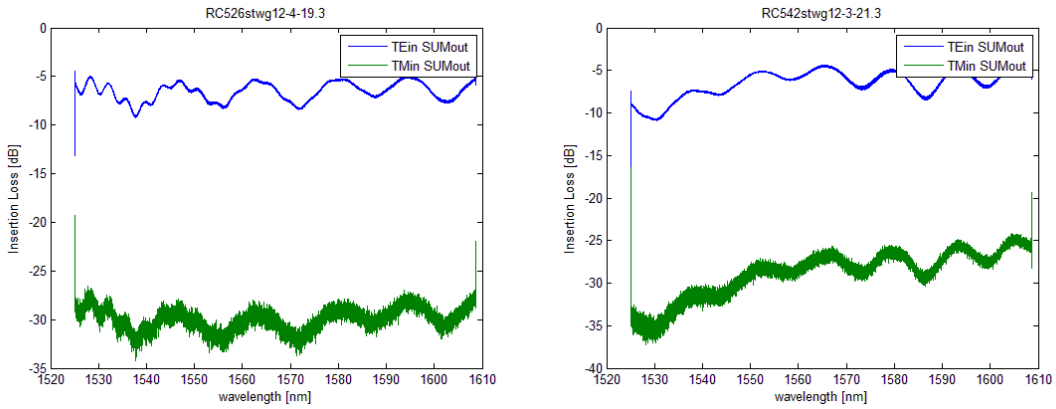

(a) (b)

Fig. 34 Initial APE fabrication results. a) Sample RC526 was exchanged for 20 minutes at 200°C. The anneal step was processed at 393°C for 5 hours. b) Sample RC542 was fabricated for 25 minutes at 200°C. It was annealed at 391°C for 5 hours.

Table VIII
APE fabrication parameters for samples RC526 & RC542

Sample	Exchange Time	Exchange Temperature	Anneal Time	Anneal Temperature
RC526	20 min	200°C	5 hr	393°C
RC542	25 min	200°C	5 hr	391°C

Initial APE fabrication trials were performed with the parameters given in Table VIII. As can be seen from the transmission measurements in Fig. 34 above, the insertion loss ranged from 5-10 dB with an abundance of beating. This beating suggests that multiple TE modes were allowed to propagate (multimode beating). Notice that the green line, or TM mode, is virtually extinct. This is to be expected because it is a typical result of x-cut y-propagating APE waveguides that decrease the value of n_o. The anneal step for these two samples used the same parameters, with the only difference being the exchange time. Sample RC542 was exchanged 5 minutes longer and has noticeably more insertion loss. This can be attributed to the higher proton concentration in the exchanged region.

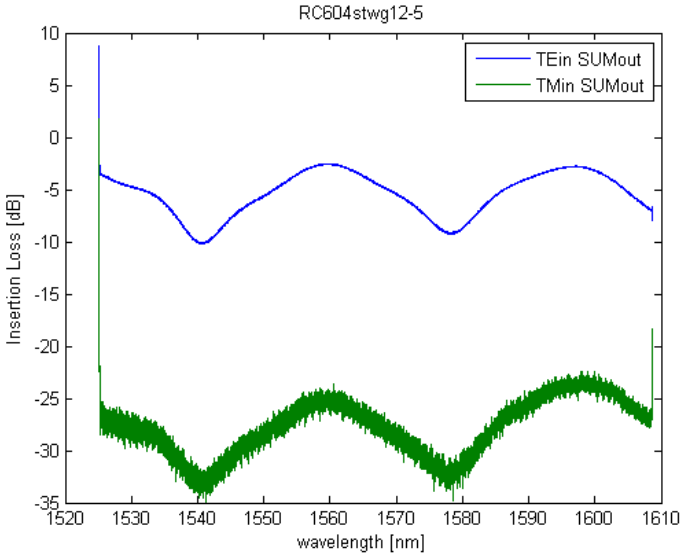

Fig. 35 APE fabrication results for sample RC604. Exchanged for 30 minutes at 201°C. The anneal step was processed at 392°C for 4.25 hours.

Table IX
APE fabrication parameters for sample RC604

Sample	Exchange Time	Exchange Temperature	Anneal Time	Anneal Temperature
RC604	30 min	201°C	4.25 hr	392°C

A new sample was fabricated at the same exchange and anneal temperatures as the previous samples, but with a longer exchange time and shorter anneal time Table IX. From Fig. 35 above, it can be seen that there is better insertion loss, but there is still some multimode beating. The beating is more sinusoidal in nature than samples RC526 and RC542s sporadic behavior, which leads one to believe that sample RC604 allows only two TE modes to propagate.

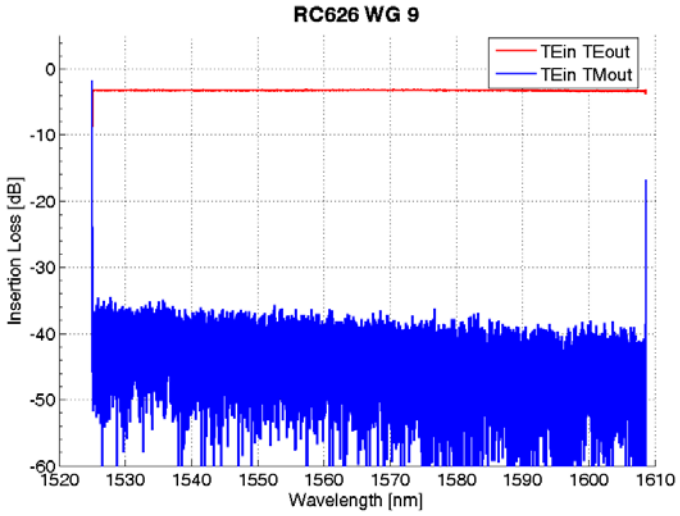

Fig. 36 APE fabrication results for sample RC626. Exchanged for 20 minutes at 200°C. The anneal step was processed at 400°C for 3.5 hours.

Table X
APE fabrication parameters for sample RC626

Sample	Exchange Time	Exchange Temperature	Anneal Time	Anneal Temperature
RC626	20 min	200°C	3.5 hr	400°C

Sample RC626 was fabricated with the same proton exchange parameters as RC526, but with a shorter anneal time and slightly higher anneal temperature, Table X. As can be seen in Fig. 36 above, the extinction ratio between TE and TM modes is greater than that of previous samples, but the most important difference is the fact that the response is flat throughout the entire wavelength range. This illustrates that the APE waveguide is single mode, which is desired. Although this is the best result so far, the insertion loss is not as low as wanted. Other APE sample fabrication results can be found in Table XI below. This led to an incremental anneal experiment.

Table XI
APE fabrication results for various samples

Sample	Exchange Time (min)	Exchange Temp. (°C)	Anneal Time (hrs)	Anneal Temp. (°C)	Insertion Loss (dB)
RC642	21	201	5	391	8
RC645	21.5	200	4	391	7.5
RC604	30	201	4.25	391.8	8.5
RC526	20	201	5	393	4
RC583	15.5	201	4	395	5
RC650	27	200	3.5	399.5	4
RC655	31	200	3.5	399.5	4.5
RC626	20	200	3.5	400.5	3.5
RC614	20.5	201	3.5	400.5	3.5
RC670	25.5	201	3.5	401	10
RC674	28	201	3.5	401	12.5
RC677	20.5	200	3.5	400.4	8
RC689	22.5	200	3.5	400.4	10

A.2. Incremental Anneal

Two samples were fabricated in this experiment with PE parameters as seen in Table XII. Once samples RC668 and RC669 were exchanged, they were annealed in increments of 30 minutes. After each successive anneal they were measured with the LUNA in transmission mode and in reflection mode. Transmission mode allows for normal measurements to be carried out as in the above discussions. With reflection mode

enabled, the LUNA is able to plot the time when the light reflects off the first end, left edge of sample, and second end, right edge of sample. This information allows one to calculate the time it takes the light to travel through the sample and therefore relate that to the refractive index of the APE region.

Table XII
Incremental anneal exchange parameters & anneal temperature

Sample	Exchange Time	Exchange Temperature	Anneal Temperature
RC668	15 min	200°C	400°C
RC669	20 min	200°C	400°C

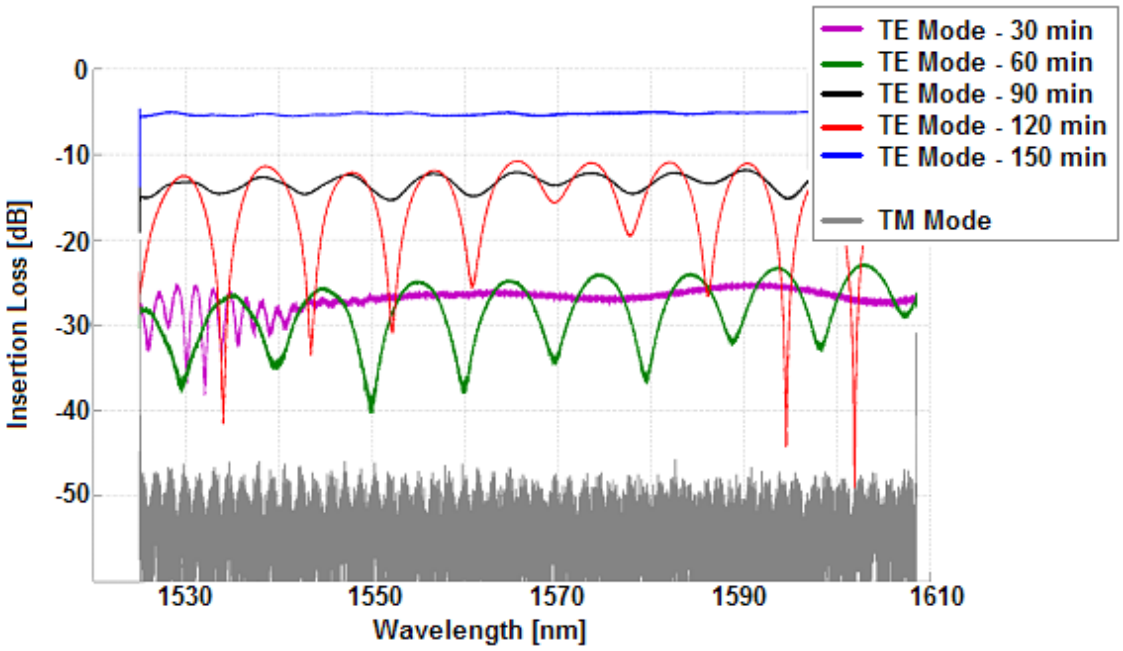

Fig. 37 Incremental anneal results for sample RC669. This sample was exchanged for 20 minutes at 200°C. It was annealed at 400°C in increments of 30 minutes from 30-150 minutes. After each anneal step the transmission spectrum was measured and is plotted here. The anneal times do not include sample cool down time.

The first sample discussed here is RC669, which was exchanged for 20 minutes. As can be seen in Fig. 37 above, after a 30 minute anneal almost no transmission is achieved. After each successive anneal the response becomes better. The diffused waveguides become multimode supportive, but continue to exhibit high losses. The losses get better after 2 hours of anneal time, but continue to support multi-modes. After 2.5 hours of anneal time the waveguides are now single-mode guides, with lower losses. These losses are around 5 dB, which is still too high.

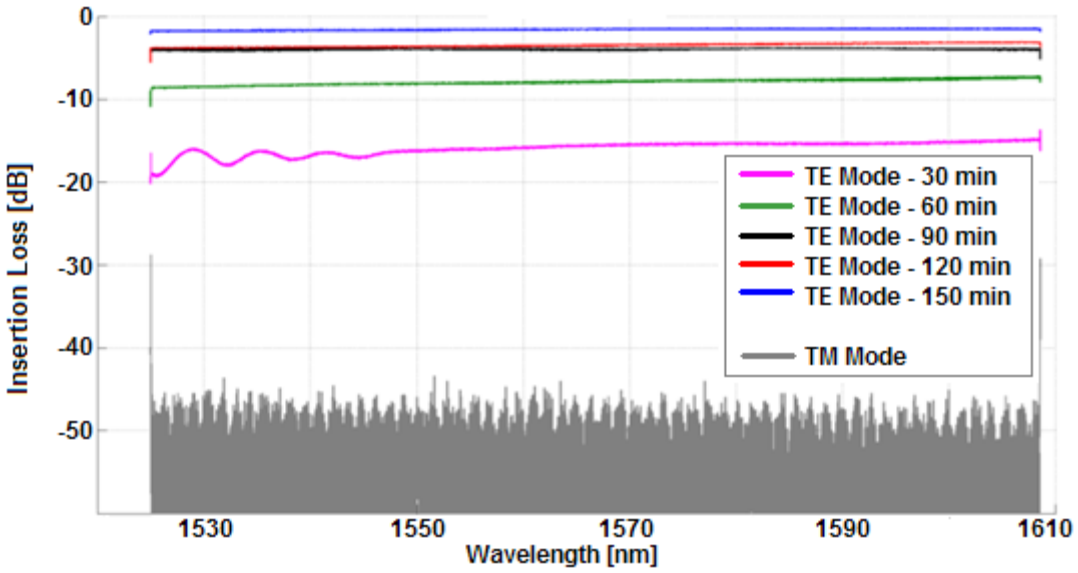

Fig. 38 Incremental anneal results for sample RC668. This sample was exchanged for 15 minutes at 200°C. It was annealed at 400°C in increments of 30 minutes from 30-150 minutes. After each anneal step the transmission spectrum was measured and is plotted here. The anneal times do not include sample cool down time.

Sample RC668 was exchanged for 15 minutes and went through the same process as RC669. After the first 30 minute anneal, this sample was already single-mode

for most wavelengths, with much better insertion loss than the previous sample. At the final 2.5 hour anneal the insertion loss was down to approximately 1.6 dB or 0.8 dB/cm, which rivals that of titanium diffused waveguides produced here. These results can be seen in Fig. 38.

The insertion losses for sample RC668 were averaged for all wavelengths and plotted against anneal time, Fig. 39. This data gives a good idea of how anneal time affects insertion loss.

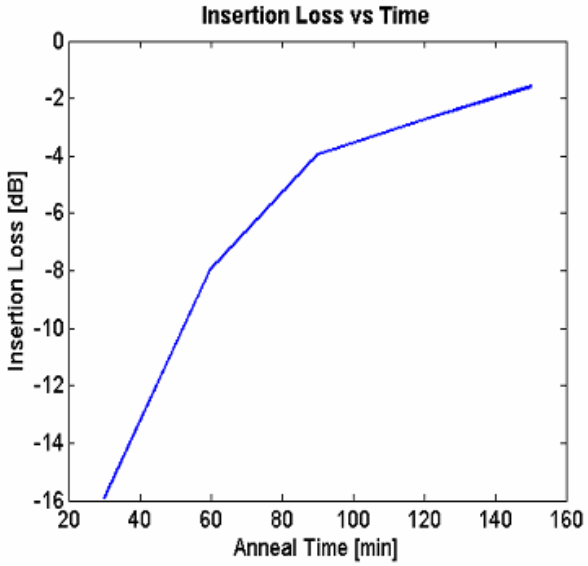

Fig. 39 Insertion loss vs. time for the incremental anneal of RC668. Values plotted are the average insertion loss for the wavelength range of 1525-1610 nm. Best loss being 1.6 dB for a 2 cm sample.

The data from Fig. 39 was subsequently fit to see if an ideal anneal time for the given PE and anneal parameters could be found. (a) of Fig. 40 was fit by an exponential function of form

$$a\exp^{(bx)} + c\exp^{(dx)} \quad . \tag{55}$$

This fit suggests that further annealing could possibly result in lower insertion losses for the parameters under question. In (b) an extra data point was added to the data from (a) of Fig. 40. This data is from sample RC664, which was fabricated with the same exchange parameters and anneal temperature as RC668. RC664 was annealed for 4 hours. A quadratic fit was used for this data and had the form

$$ax^2 + bx + c \quad . \tag{56}$$

This fit suggests that the ideal anneal time for APE samples exchanged at 200°C for 15 minutes and annealed at 400°C on x-cut lithium niobate is approximately 140 minutes.

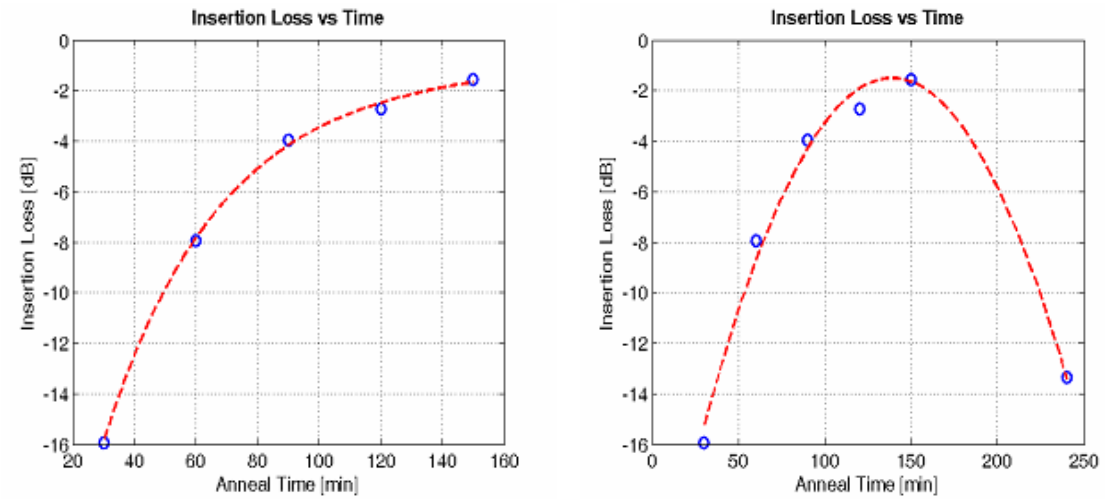

(a) (b)

Fig. 40 Fit data from the incremental anneal of RC668. a) Fit data suggesting that further annealing could reduce insertion loss even more. b) Fit data with extra data point added from RC664 which underwent same exchange and anneal conditions as RC668, but was annealed for 240 minutes.

As stated above, RC668 was also measured in reflection mode and the results can be found in Fig. 41. The time domain peak on the left side of the figure represents when the light was reflected from the left edge of the sample and the right peak makes the analogous representation of the light that has been transmitted through the sample and reflected from the right edge.

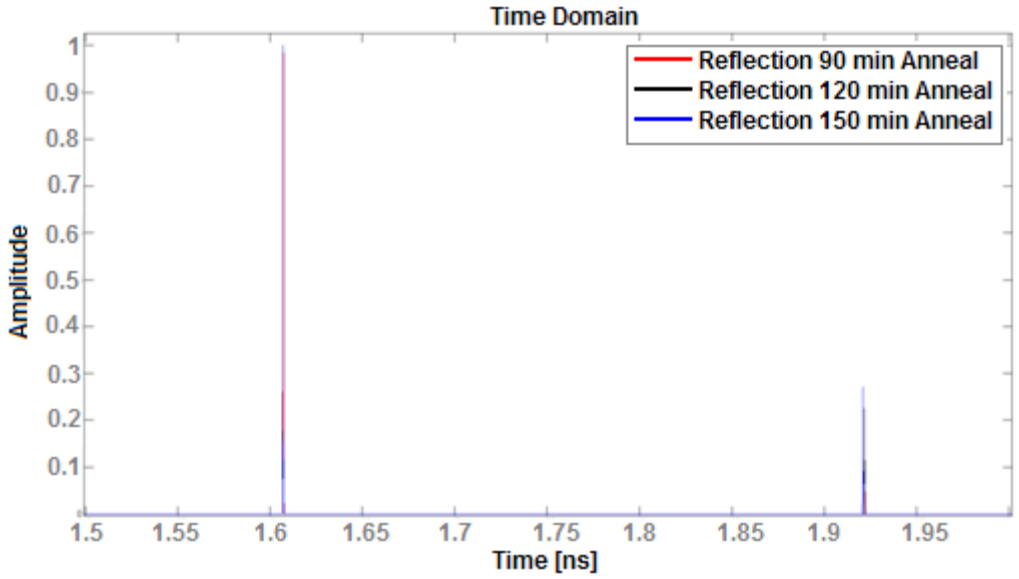

Fig. 41 Time Domain plot for RC668 measured in reflection mode. The peak on the left side of the image is when the light reflects from the left edge of the device under test (DUT) and the right peak represents when the light reflects from the right side of the sample. Light is moving from left to right.

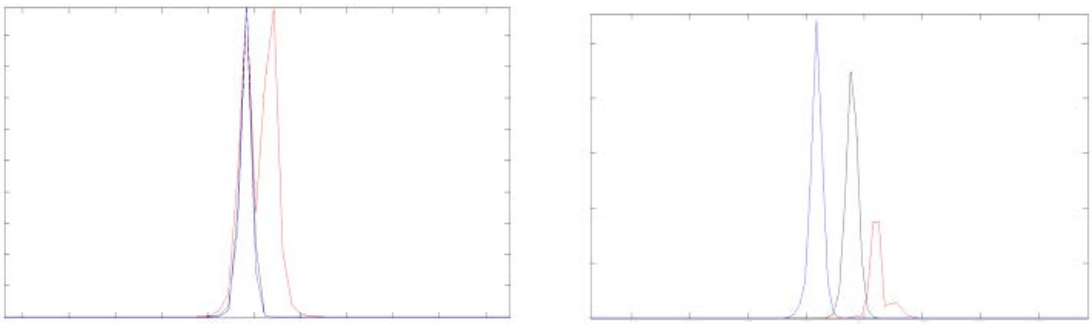

(a) (b)

Fig. 42 Time domain plot for RC668 with anneal times of 90-150 minutes. a) Left peaks of the time domain plot which are in the same place. b) Right peaks of the time domain plot which take place at different points in time suggesting a change in refractive index.

This information, along with the length of the waveguide can be used to find the refractive index of the APE region. From Fig. 42, (a) shows that the left peaks for the anneals of RC668 ranging from 90-150 minutes are in the same position and (b) shows that the right peaks occur at different points in time. In (a) there appears to be two red peaks which suggest multimode propagation, even though the spectral response plot in Fig. 38 does not exhibit mode beating. This suggests that there is a change in refractive index. By measuring the length of the sample and calculating the difference between each respective left and right peak, the following equation was used to find the refractive index.

$$n = \frac{\Delta t \times c_o}{2 \times l} \tag{57}$$

where c_o = 2.998x10^8 m/s is the speed of light and l = 2.15646 cm is the length of the sample measured with a slide caliper. The bulk index for the extraordinary ray in

$LiNbO_3$ is n_e = 2.13811. Table XIII lists the travel time, Δt, for each anneal along with its calculated refractive indices.

Table XIII
Calculated refractive indices for the incremental anneal of RC668

Anneal Time	Travel Time	Refractive Index (n)
90 min	0.315335 ns	2.1919
120 min	0.3148 ns	2.1844
150 min	0.3143 ns	2.1804

B. Mode Profile Measurements

The mode profile is measured from the ThorLabs Beam Profiler and gives interesting information about the mode intensity, how many modes are propagating, and allows one to calculate the fiber-to-waveguide mode mismatch. The setup consists of a laser that is coupled into the fabricated waveguide by optical fiber, a lens that focuses the output of the waveguide onto the beam profiler's slit, and the beam profiler which is interfaced with a computer with software that allows the visualization of the mode profile. Polarization paddles are used in order to allow full power for the TE polarization, because it is the only polarization allowed to propagate in x-cut $LiNbO_3$. In order, to obtain accurate mode characteristics, the setup must be calibrated with two straight waveguides of known spacing. The output modes from these two waveguides are measured, without moving the lens or beam profiler, and a pixel to length ratio is found using MATLAB to find the actual beam characteristics.

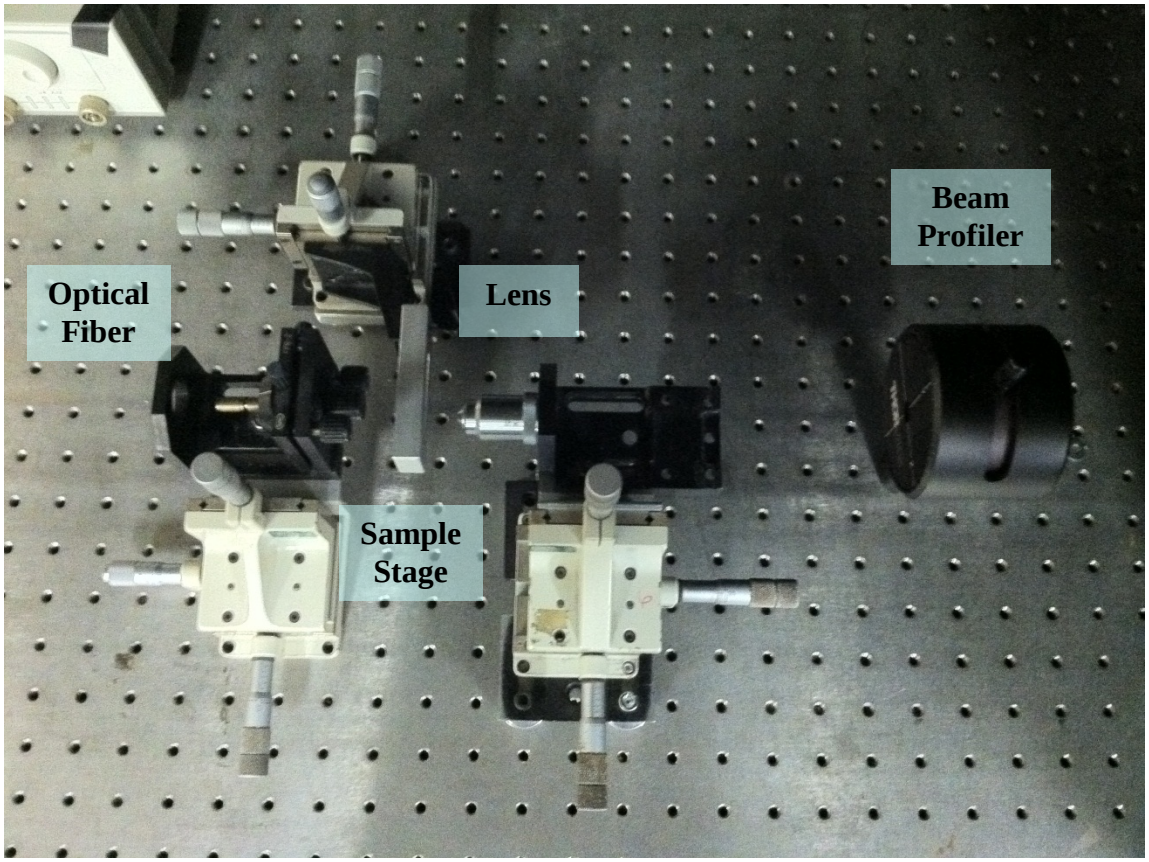

Fig. 43 Beam profile setup. Setup consists of a laser coupled to sample with an optical fiber, a lens to focus output from waveguide onto beam profiler slit, and the beam profiler interfaced with a computer and software.

Mode profiles were measured for the samples presented in the APE Waveguide Measurements section. The mode profiles for samples RC526 and RC604 can be found in Fig. 44. The transmission spectrum of RC526 shows a sporadic beating behavior which leads one to believe that more than two modes are propagating through the waveguide. As seen in the mode profile of RC526, there is a main mode with two side modes on either side. This shows that there are three TE modes propagating and confirms the previous assumptions. Sample RC604's transmission spectrum was more of

a sinusoidal beating which is evident in waveguides supporting two modes. This, again, is proven with RC604's mode profile where two modes can be seen.

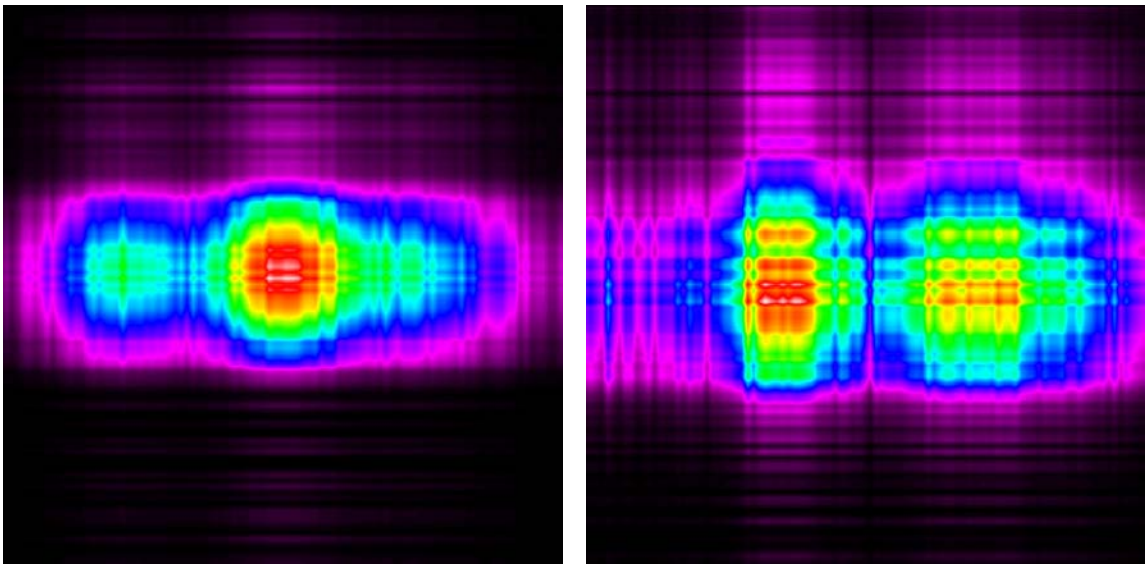

(a) (b)

Fig. 44 Mode Profiles for initial APE fabrication. a) Mode Profile for sample RC526 with a main mode and two side lobes suggesting three modes of propagation. b) Mode profile for sample RC604 suggesting two modes of propagation.

The transmission spectrum of RC626 was smooth for the entire range from 1525-1610 nm, but had insertion losses that were higher than desired. From the mode profile in Fig. 45, it can be seen that there is single mode propagation. The data from the beam profiler was entered into MATLAB where the mismatch factor (η), mismatch/coupling loss, and mode field diameter (MFD) were found with the fiber mode of a single mode fiber taken as 10.7 μm. The same was done for sample RC668 after the final anneal. The results are compared in Table XIV. As seen, some of the extra loss exhibited by RC 626

is from mode mismatch which is much greater than that for RC668. Removing this mismatch loss from the insertion loss yields a propagation loss value of approximately 0.2 dB/cm.

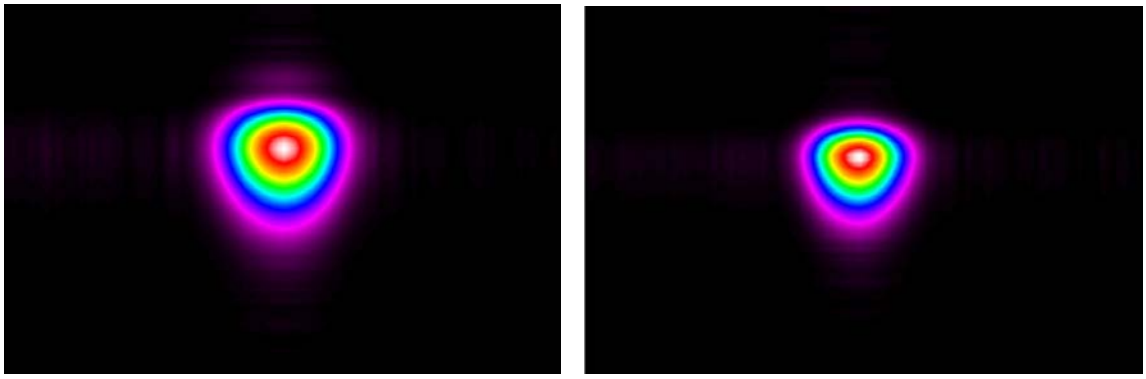

(a) (b)

Fig. 45 Mode Profiles for samples RC626 and RC668. a) Mode profile for RC626 which exhibits single mode propagation and a MFD of 17.21. b) Mode profile of RC668 which has single mode propagation and ideal MFD of 10.66.

Table XIV
Mode properties for RC626 and RC668

	RC626	RC668
Horizontal beam width (μm)	18.725	11.834
Vertical beam width (μm)	15.814	9.605
Mismatch factor	79.16%	93.59%
Mismatch Loss (dB)	1.0149	0.288
Mode field diameter (μm)	17.2081	10.661

C. Surface Profile Measurements

A major advantage of using APE waveguides of Ti:$LiNbO_3$ waveguides is a reduction of the surface bump from the bus waveguide. Ti:$LiNbO_3$ waveguides have a post diffusion bump of approximately two times the initial Ti film deposition, resulting in an approximately 200 nm step height. APE waveguides will not have this. An oxide mask layer must be patterned before doing proton exchange, and the waveguide openings can be etched in two ways as described in Chapter 4. Wet etching has a fast etch rate of SiO_2 which results in over etching of the fabricated channels, making them wider than desired with limited control over their width. Dry etching or plasma etching can cause over etching into the substrate, resulting in a small surface dip. An indention has been measured at only approximately 20 nm which is a 90% reduction in the bump exhibited by Ti:$LiNbO_3$. This study was carried out using a Dektak surface profilometer with results in Fig. 46.

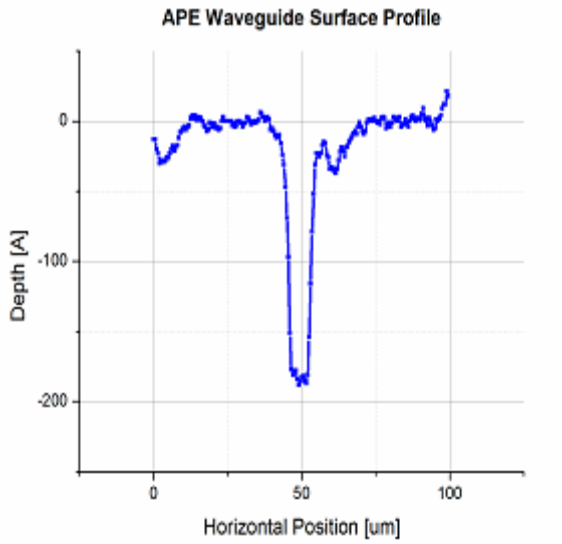

Fig. 46 Surface profile measurement of an APE waveguide.

As is evident from the SEMs in Fig. 47 below, the Ti bus waveguide exhibits a large bump whereas there is no visible sign of the APE bus waveguide under the As_2S_3.

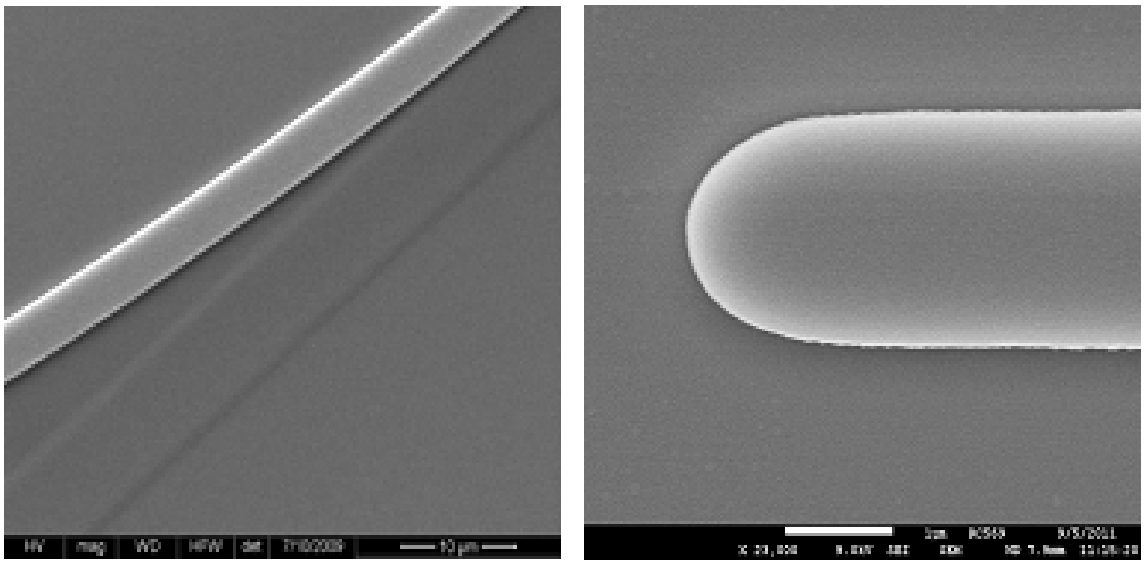

(a) (b)

Fig. 47 SEM of Ti and APE waveguides. a) SEM showing Ti bus waveguide bump with As_2S_3 rib waveguide side coupled. b) As_2S_3 rib waveguide vertically coupled on APE bus waveguide. No visible bump is noticeable.

D. Coupling Measurements

As_2S_3 MZI rib waveguides were designed with the parameters in Table XV. Using an APE bus waveguide fabricated with results found from the incremental anneal, As_2S_3 MZI waveguides were fabricated on top for vertical coupling. The LUNA was used to measure the transmission spectrum in the wavelength range of 1525-1610 nm.

Table XV
Parameters for As_2S_3 MZI structure

Parameters	
As_2S_3 thickness	0.31 μm
Taper tip width	1.0 μm
Taper length	2000 μm
Path width	3.5 μm

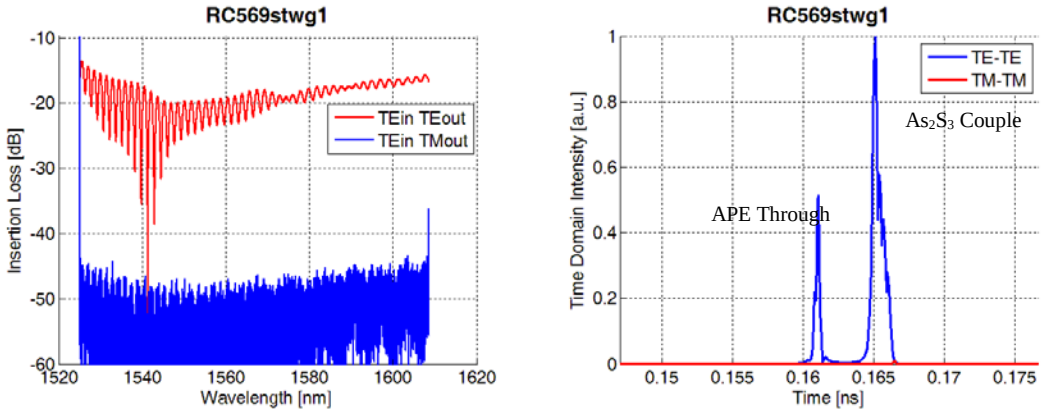

(a) (b)

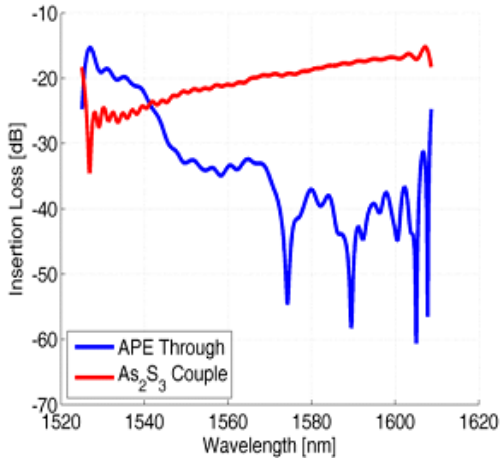

(c)

Fig. 48 MZI results for APE and As_2S_3 vertically integrated waveguides. a) Transmission spectrum from 1525-1610 nm. b) Time domain plot of MZI results showing coupling. The first peak is from the APE waveguide and the second peak is from the As_2S_3 waveguide. c) Power measurements from each individual branch of the MZI structure.

Image (a) from Fig. 48 shows a typical MZI response with a weaker response at higher wavelengths. The second image, time domain response of the APE MZI structure displays two different peaks. This proves that there is coupling in that the light is split

and travels through each of the branches of the MZI structure, with the light traveling in the higher indexed, longer path length As_2S_3 rib waveguide arriving after that of the straight APE bus waveguide. Also, as can be seen from the intensity value, there is high coupling to the As_2S_3 waveguide. This is a much higher coupling ratio than is exhibited by vertically integrated MZI structures fabricated on titanium diffused waveguides.

From the time domain plot, each path can be separated to look at its individual spectral response. From Fig. 48 (c) As_2S_3 coupling is observed at a longer wavelength than the Ti:$LiNbO_3$ case. This is believed to be due to the As_2S_3 taper tip width being larger than desired. Taper tip width is a major limitation of contact lithography which has a feature limit of around 1 μm.

To establish that coupling is truly taking place, calculations were carried out to estimate the change in time, Δt, for the light traveled in each branch, as depicted in Fig. 48 (b).

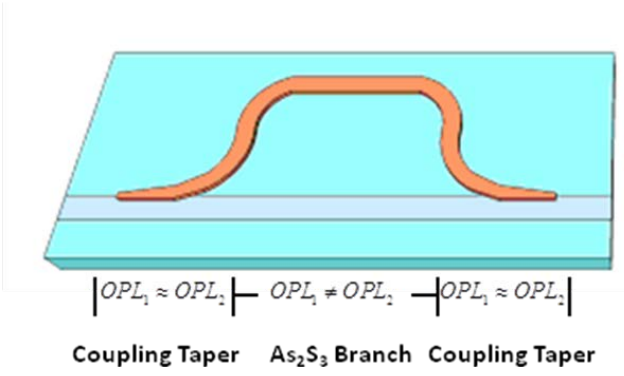

Fig. 49 MZI structure showing where the optical path lengths are estimated the same and where it is different.

Using the structure in Fig. 49, the optical path length can be defined as

$$OPL = n \times l \ , \tag{58}$$

where n is the refractive index and l is the physical path length. From (58), one can infer that the optical path difference (OPD) is

$$OPD = \left| n_1 l_1 - n_2 l_2 \right|, \tag{59}$$

where n_1 = 2.15, l_1 = 5.7 mm, n_2 = 2.25, l_2 = 5.75 mm. Using $\Delta\phi = k_o \left(OPD \right)$, $k_o = \frac{2\pi}{\lambda_o}$, $\Delta f = \frac{c_o}{OPD}$, and $T = \frac{1}{\Delta f}$, the change in time can be calculated from

$$\Delta t = \frac{OPD}{c_o} \ , \tag{60}$$

This gives us a Δt of 0.006 ns, which is in agreement with the time domain spectral response.

CHAPTER VI

CONCLUSIONS

Procedures for annealed proton-exchanged (APE) waveguides have been developed through simulations and experimental results. These have led to the fabrication of low-loss waveguides with propagation loss of approximately 0.2 dB/cm. After these APE waveguides were fabricated, vertically integrated chalcogenide rib waveguides were fabricated on top. Through spectral measurements, it has been shown that these devices exhibit coupling with high coupling ratios. These are the first reported coupling results for vertically integrated chalcogenide rib waveguides on top of annealed proton-exchanged bus waveguides.

A. Future Work

The diffusion properties for annealed proton-exchanged waveguides are highly dependent on experimental setups and many other variable factors. Because of this, the modeling of APE waveguides is not as accurate as it should be. In order to get more precise results with modeling and simulations, the exact diffusion parameters for the benzoic acid used here need to be characterized.

This can be achieved by exchanging several samples at the same temperature for different amounts of time. For example, five samples could be exchanged at 200°C from 5-25 minutes. When this is complete, a measurement technique such as SIMS or X-ray diffraction can be used to find the hydrogen concentration for each of the five exchange

times. The Arrhenius equation can then be solved to find the diffusion constants. This would give better results on modeling the exchange process. The same can be done with the anneal process and then both of these cases combined could lead to better results when coupled with As_2S_3 rib waveguides.

Once this is achieved, a new lithography technique could be employed. Techniques such as projection lithography or electron beam lithography will help with the fabrication of smaller taper tip widths for the As_2S_3 MZI structures. It has been shown through simulations that taper tip widths of 0.8 μm and smaller are ideal for coupling the TE mode into the vertically integrated chalcogenide.

After smaller taper tip widths come to fruition, the vertical integration can move forward to fabricating ring resonator structures on top of APE bus waveguides. This poses a problem, though. As explained in Chapter 2 and given by (25), the TE mode's refractive index is dependent on the angle. The rings are perpendicular to the APE bus waveguide at two points, which makes $\theta = 90°$ at these two places. This causes the TE mode to see n_o at those points, decreasing the confinement and causing the light to radiate into the substrate producing extremely high losses. The TM mode is the vertical mode in this case so it is independent of the angle, but the TE mode is the horizontal mode so it sees the index change with the angle.

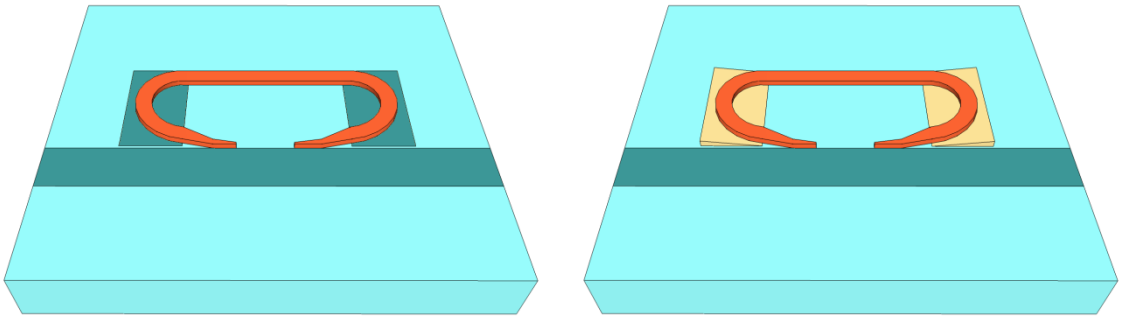

(a) (b)

Fig. 50 Ring resonator fabrication ideas for TE mode waveguides. a) Ring resonator structure with PE openings under the ring bend regions. b) Ring resonator structure with nano-ramps fabricated under ring bend regions

To combat this, the fact that PE decreases the value of n_o can be used. Fabrication of proton exchanged openings can be completed in the bending regions of the ring resonator in order to have a more favorable refractive index for the TE mode as in the APE straight waveguide regions, Fig. 50 (a). Another way to work around this index dilemma is to fabricate micro-ramps, Fig. 50 (b). These ramps would be fabricated before the chalcogenide and would be placed in a similar fashion as the PE openings. A material such as SiO_2 can be used for the ramp. During the fabrication process, the sample could be exposed at an angle or the use of shadow mask deposition could be employed in order to create these ramps. This would effectively pull the mode out of the $LiNbO_3$ substrate so that it would not see n_o. The ramp structure would be needed in order to prevent another occurrence of a surface bump as in titanium indiffused waveguides.

REFERENCES

[1] R. V. Schmidt and I. P. Kaminow, “Metal-diffused optical waveguides in $LiNbO_3$,” *Appl. Phys. Lett.*, vol. 25, no. 8, pp. 458-460, Oct. 1974.

[2] J. L. Jackel, C. E. Rice, and J. J. Veselka, “Proton exchange for high-index waveguides in $LiNbO_3$,” *Appl. Phys. Lett.*, vol. 41, no. 7, pp. 607-608, Oct. 1982.

[3] D. K. Cheng, Fundamentals of Engineering Electromagnetics. New Jersey: Prentice Hall, 1993.

[4] R. S. Weis and T. K. Gaylord, “Lithium niobate: Summary of physical properties and crystal structure,” *Appl. Phys. A*, vol. 37, no. 4, pp. 191-203, Aug. 1985.

[5] K. Nassau and H. J. Levinstein, “Ferroelectric behavior of lithium niobate,” *Appl. Phys. Lett.*, vol. 7, no. 3, pp. 69-70, Aug. 1965.

[6] H. Nishihara, M. Haruna, and T. Suhara, Optical Integrated Circuits. New York: McGraw-Hill, 1989.

[7] L. Arizmendi, “Photonic applications of lithium niobate crystals,” *Phys. Stat. Sol.* (a), vol. 201, no. 2, pp. 253-283, Jan. 2004.

[8] D. E. Zelmon, D. L. Small, and D. Jundt, “Infrared corrected sellmeier coefficients for congruently grown lithium niobate and 5 mol. % magnesium oxide-doped lithium niobate,” *J. Opt. Soc. Am. B*, vol. 14, no. 12, pp. 3319-3322, December 1997.

[9] D. S. Smith, H. D. Riccius, and R. P. Edwin, “Refractive indices of lithium niobate,” *Opt. Comm.*, vol. 17, no. 3, pp. 332-335, Jun. 1976.

[10] G. J. Edwards and M. Lawrence, "A temperature-dependent dispersion equation for congruently grown lithium niobate," *Opt. and Quant. Elec.*, vol. 16, no. 4, pp. 373-375, Jul. 1984.

[11] E. H. Turner, “High-frequency electro-optic coefficients of lithium niobate,” *Appl. Phys. Lett.*, vol. 8, no. 11, pp. 303-304, June 1966.

[12] E. A. J. Marcatili, “Dielectric rectangular waveguide and directional coupler for integrated optics,” *Bell Systems Technology Journal*, vol. 48, no. 21, pp. 2071-2102, Sep. 1969.

[13] R. M. Knox and P. P. Toulios, “Integrated circuits for the millimeter through optical frequency range,” presented at the Symposium on Submillimeter Waves, Polytechnic Institute of Brooklyn, 1970.

[14] C. T. Lee, M. L. Wu, L. G. Sheu, P. L. Fan, and J. M. Hsu, “Design and analysis of completely adiabatic tapered waveguides by conformal mapping,” *J. Light Tech.*, vol. 15, no. 2, pp. 403-410, Feb. 1997.

[15] M. E. Solmaz, D. B. Adams, S. Grover, W. C. Tan, X. Xia, et *al*., “Compact bends for achieving higher integration densities for $LiNbO_3$ waveguides,” *Phot. Tech. Lett.*, vol. 21, no. 9, pp. 557-559, May 2009.

[16] M. Fukuma and J. Noda, “Optical properties of titanium-diffused $LiNbO_3$ strip waveguides and their coupling-to-a-fiber characteristics,” *Appl. Opt.*, vol. 19, no. 4, pp. 591-597, February 1980.

[17] M. Fukuma, J. Noda, and H. Iwasaki, “Optical properties in titanium-diffused $LiNbO_3$ strip waveguides,” *J. Appl. Phys.*, vol. 49, no. 7, pp. 3693-3698, July 1978.

[18] R. C. Alferness, “Titanium diffused waveguide devices,” *Applications of Ferroelectrics. 1986 Sixth IEEE International Symposium on*, pp. 1-3, 1986.

[19] P. G. Suchoski, T. K. Findakly, and F. J. Leonberger, “Stable low-loss proton-exchanged $LiNbO_3$ waveguide devices with no electro-optic degradation,” *Opt. Lett.*, vol. 13, no. 11, pp. 1050-1052, November 1988.

[20] M. E. Solmaz, D. B. Adams, W. C. Tan, W. T. Snider, and C. K. Madsen, “Vertically integrated As_2S_3 ring resonator on $LiNbO_3$,” *Opt. Lett.*, vol. 34, no. 11, pp. 1735-1737, June 2009.

[21] P. Nekvindova, J. Spirkova, J. Cervena, M. Budnar, A. Razpet, et *al.*, “Annealed proton exchanged waveguides in lithium niobate: Differences between the x- and z-cuts,” *Opt. Mat.*, vol. 19, pp. 245-253, 2002.

[22] J. L. Jackel, C. E. Rice, J. J. Veselka, “Proton exchange for high-index waveguides in $LiNbO_3$,” *Appl. Phys. Lett.*, vol. 41, no. 7, pp. 607-608, October 1982.

[23] J. Olivares, M. A. Diaz-Garcia, and J. M. Cabrera, “Direct measurement of ordinary refractive index of proton exchanged $LiNbO_3$ waveguides,” *Opt. Comm.*, vol. 92, no. 1, pp. 40-44, August 1992.

[24] I. V. Il'ichev, A. S. Koslov, P. V. Gaenko, and A. V. Shamrai, "Optimisation of the proton-exchange technology for fabricating channel waveguides in lithium niobate crystals," *Quant. Elec.*, vol. 39, no.1, pp. 98-104, 2009.

[25] Y. N. Korkishko, V. A. Fedorov, O. Y. Feoktistova, and T. V. Morozova, "Effect of SiO_2 cladding on properties of annealed proton-exchanged $LiNbO_3$ waveguides," *J. Appl. Phys.*, vol. 87, no. 9, pp. 4404-4409, 2000.

[26] A. Yi-Yan, "Index instabilities in proton-exchanged $LiNbO_3$ waveguides," *App. Phys. Lett.*, vol. 42, no. 8, pp. 633-635, April 1983.

[27] R. A. Becker, "Comparison of guided-wave interferometric modulators fabricated on $LiNbO_3$ via Ti indiffusion and proton exchange," *App. Phys. Lett.*, vol. 43, no. 2, pp. 131-133, July 1983.

[28] J. L. Jackel, C. E. Rice, and J. J. Veselka, "Composition control in proton-exchanged $LiNbO_3$," *Elec. Lett.*, vol. 19, no. 10, pp. 387-388, 1983.

[29] Y. N. Korkishko, V. A. Fedorov, E. A. Baranov, M. V. Proyaeva, and T. V. Morozova, "Characterization of α-phase soft proton-exchanged $LiNbO_3$ optical waveguides," *J. Opt. Soc. Am. A*, vol. 18, no. 5, May 2001.

[30] M. Howerton, W. K. Burns, P. R. Skeath, A. S. Greenblatt, "Dependence of refractive index on hydrogen concentration on proton exchanged $LiNbO_3$," *J. Quant. Elec.*, vol. 27, no. 3, pp. 593-601, Mar. 1991.

[31] J. Rams and J. M. Cabrera, "Preparation of proton-exchange $LiNbO_3$ waveguides in benzoic acid vapor," *J. Opt. Soc. Am. B*, vol. 16, no. 3, pp. 401-406, March 1999.

[32] M. De Micheli, J. Botineau, S. Neveu, P. Sibillot, and D. B. Ostrowsky, "Independent control of index profiles in proton-exchanged lithium niobate guides," *Opt. Lett.*, vol. 8, no. 2, pp. 114-115, February 1983.

[33] J. L. Jackel and J. J. Johnson, "Reverse exchange method for burying proton exchanged waveguides," *Elec. Lett.*, vol. 27, no. 15, pp. 1360-1361, July 1991.

[34] Y. N. Korkishko, V. A. Fedorov, T. M. Morozova, F. Caccavale, F. Gonella, et *al.*, "Reverse proton exchange for buried waveguides in $LiNbO_3$," *J. Opt. Soc. Am. A*, vol. 15, no. 7, pp. 1838-1842, July 1998.

[35] K. K. Wong, A. C. G. Nutt, D. F. Clark, J. Winfield, P. J. R. Laybourn, et *al.*, " Characterisation of proton-exchange slab optical waveguides in x-cut $LiNbO_3$," *IEEE Proc.*, vol. 133, no. 2, pp. 113-117, Apr. 1986.

[36] J. M. M. M. de Almeida, “Design methodology of annealed H^+ waveguides in ferroelectric $LiNbO_3$,” *Opt. Eng.*, vol. 46, no. 6, pp. 1-13, June 2007, paper 064601.

[37] A. Loni, “An experimental study of proton exchanged lithium niobate optical waveguides,” PhD Thesis, Univ. of Glasgow, 1987.

[38] J. M. Zavada, H. C. Casey, C. Chen, A. Loni, “Correlation of refractive index profiles with substitutional hydrogen concentrations in annealed proton-exchanged $LiNbO_3$ waveguides,” *App. Phys. Lett.*, vol. 62, no. 22, pp. 2769-2771, May 1993.

[39] L. McCaughan and E. J. Murphy, “Influence of temperature and initial titanium dimensions on fiber-Ti:$LiNbO_3$ waveguide insertion loss at $\lambda = 1.3$ μm,” *J. Quant. Elec.*, vol. 19, no. 2, pp. 131-136, Feb. 1983.

APPENDIX A

FABRICATION PROCESS

- **SiO_2 Mask Layer Deposition**
  - Sputter 2000 Å SiO_2 on $LiNbO_3$ substrate

- **Lithoghraphy**
  - Clean Sample
    - *Rinse w/ acetone*
    - *Rinse w/ methanol*
    - *Rinse w/ isopropanol*
    - *Dry w/ N_2*
  - Apply Photoresist
    - *Spin AZ5214 @ 4000 RPM for 40 sec w/ 5 sec ramp up/ramp down time*
    - *Soft bake on hotplate for 1 min @ 125°C*
  - Photolithography
    - *Align waveguides w/ sample*
    - *Expose @ 85 mJ/cm^2*
    - *Develop w/ MF312 for ~55 sec*
      - *6 parts DI-water*
      - *5 parts MF312 Developer*
    - *Check under microscope that development is complete if not develop longer*
    - *Hard bake for 8 min @ 135°C*

- **Etch**
  - Use RIE to open channels in SiO_2
  - Remove undeveloped photoresist with AZ300T photoresist stripper

- **Proton Exchange**
  - Fill 100 mL beaker with 60-80 mL of benzoic acid and cover with Al foil
  - Fill 300 mL beaker with DI-water
  - Place on hotplate and set temp. @ 200°C
    - *Place thermal probe in water until BA is melted*
    - *Wait ~20 min for BA to melt*
  - Place magnetic stirrer in BA melt
    - *Stir @ 60 RPM*
  - Cover BA beaker with insulator sleeve
    - *Place thermal probe in lid opening of sleeve so that it is immersed in the BA melt*
  - When BA reaches 200°C place sample on sample holder
    - *Hold above acid for 1-2 min to avoid temperature shock*
  - Place sample in BA for 15 min
    - *close thermal sleeve with clamp*
  - Remove sample from BA
    - *Hold above acid for 1-2 min to avoid temperature shock*
    - *Place on beta wipe and wait until cooled to room temp*
    - *turn off hotplate and dispose of BA*
  - Clean sample with isopropanol
    - *If benzoic acid remains on sample use q-tip to remove*
    - *Dry w/ N_2*

- **Anneal**
  - Before PE process turn on diffusion furnace
    - *Set to 400°C, settings: 124, 124, 124*
    - *Flow wet breathing air @ 30 sccm*
  - Place sample on boat
    - *Set boat in furnace @ the edge for ~5 min*
    - *Slowly push boat with quartz rod to center of furnace to avoid temperature shock*
  - Anneal for 2.5 hrs @ 400°C
    - *After time has expired turn off furnace and air flow*
    - *Allow to cool to room temp ~4 hrs*
  - Remove from furnace

- **Polish Sample**
  - Turn on DI-water flow
  - Polish samples with diamond grit polishing pads while checking sample progress after each step
    - *15 µm pad: 2 min @ 135 RPM*
    - *3 µm pad: 2 min @ 85 RPM*
    - *0.5 µm pad: 2 min @ 55 RPM*
  - Clean sample with acetone, methanol, and isopropanol. Dry with N_2

- **As_2S_3/Protective Layer Deposistion**
  - Sputter 280-310 nm As_2S_3 on APE:$LiNbO_3$ substrate
  - Deposit 1500 Å SiO_2
  - Deposit 200 Å Ti

- **Lithography**
  - Clean Sample
    - *Rinse w/ acetone*
    - *Rinse w/ methanol*
    - *Rinse w/ isopropanol*
    - *Dry w/ N_2*
  - Apply Photoresist
    - *Spin AZ5214 @ 7000 RPM for 40 sec w/ 5 sec ramp up/ramp down time*
    - *Soft bake on hotplate for 1 min @ 125°C*
  - Photolithography
    - *Align waveguides w/ alignment marks on sample*
    - *Expose @ 85 mJ/cm^2*
    - *Develop w/ MF312 for ~55 sec*
      - *6 parts DI-water*
      - *5 parts MF312 Developer*
    - *Check under microscope that development is complete if not develop longer*
    - *Hard bake for 30 min @ 135°C*

- **Etch**
  - Use RIE to etch As_2S_3/Protective Layer
  - Remove undeveloped photoresist with O_2 ashing

APPENDIX B

MATLAB Code for APE Waveguide Simulations

```
clc;
clear all, close all;

%% Change Settings

% Exchange Region
width = 7;  % um

% Anneal Temperature
TC= 400;    % deg C
% Anneal Time
t= 2.5;       % hours

% Exchange Temperature
t1= 200;    % deg C


%% PE initial step Diffusion Coeff II

%***constants from Almeida et al.
% Do= 0.48e8; %um^2/hr for Benzoic Acid
% Q= 77.4e3; %J/mol
% R= 8.3144621; %J/(mol*K)

%***constants from Wong et al.
% Do= 4.326e8; %um^2/hr for Benzoic Acid
% Q= 84e3; %J/mol
% R= 8.3144621; %J/(mol*K)

    %***constants from Loni
%Do= 1.5e8; %um^2/hr for Benzoic Acid
%Q= 79.3e3; %J/mol
%R= 8.3144621; %J/(mol*K)

    %***constants from experiments
Do= 0.7725e8; %um^2/hr for Benzoic Acid
Q= 79.3e3; %J/mol
R= 8.3144621; %J/(mol*K)

TCe=160:260;
T= TCe+273.15;
De= Do*exp(-Q./(R*T));

figure()
```

```
set(gca,'FontSize',14)
plot(TCe,De)
grid on
Title('H^+ proton diffusion of Benzoic Acid in LiNbO3, x dir
(Almeida,2007)');
xlabel('Temp deg \circC');
ylabel('Diffusion Coff De [\mum^2/h]');
%% PE step depth estimate
te= 1:60;  %time (min)
de=sqrt(4*De(t1-159)*te/60);

figure()
set(gca,'FontSize',14)
plot(te,de)
grid on
xlabel('Exchange time [min]'),ylabel('d_e [\mum]');
title(['Diffusion depth of PE in pure BA at ',num2str(t1),'\circC,
(Almeida,2007)']);

dummy = input('Select data point for diffusion, p1');

%% Annealed index in X and Z direction
%use diffusion coefficients from Almeida 2007
%Samples are X cut, y propagating.  Diffusion toward mask borders is in
z direction
%need a vector for x and y directions, distribution is a product of the
two

K= 8.617385e-5; %Boltzman const, [eV/K]
lambda=1531e-3;  %wavelength in um
%modified Sellmier EQ
ne= sqrt(4.5820- 0.099169/(0.04432-lambda^2) -0.021950*lambda^2);
nsub= ne; %substrate index (n_e extraordinary), (from Abouelleil 1989)
dn_pp= 0.125;  %wavelength dependent index change for initial PE layer,
1550nm

h= p1.Position(2);  %initial exchange depth [um](same as 'de')

w= width/2; %divide width by 2
T= TC+273.15;

% ---------- Almeida findings, Xcut diffusion
Dox= 22.0e12;  %x cut diffusion coeff[um^2/h],as reported by Almeida
Hx= 1.77;  %eV
Dx= Dox*exp(-Hx/(K*T));
% ---------- Almeida findings, Z direction diffusion
Doz= 0.44e12;  %z cut diffusion coeff[um^2/h],as reported by Almeida
Hz= 1.5;  %eV,   %1.77 yields square profile
Dz= Doz*exp(-Hz/(K*T));

% % ---------- Almeida, Xcut diffusion
% Dox= 0.27e12;  %x cut diffusion coeff[um^2/h],as reported by Almeida
```

```
% Hx= 1.44;  %eV
% Dx= Dox*exp(-Hx/(K*T));
% % ---------- Almeida, Z direction diffusion
% Doz= 0.01e12;  %z cut diffusion coeff[um^2/h],as reported by Almeida
% Hz= 1.21;  %eV
% Dz= Doz*exp(-Hz/(K*T));

% length(y)
Co= 0.8;

dd= 0.05;  %increment value for x and z directions

dx= 2*sqrt(Dx*t);
dz= 2*sqrt(Dz*t);
z= -3*w:dd:3*w; %plot 2x the mask width since the H+ also diffuse in y
direction

x= 0:dd:(h+dx)*2;

Cz= erf( (w-z)/dz) + erf( (w+z)/dz);
Cx= erf( (h-x)/dx) + erf( (h+x)/dx);

figure()
set(gca,'FontSize',14)
plot(z,Cz*Co/2);title('Index distribution in Z direction');
grid on
ylabel('Index');xlabel('Diffusion in Z direction');
figure()
set(gca,'FontSize',14)
plot(x,Cx/2);
grid on
title('Index distribution in X direction');
ylabel('Index');xlabel('Diffusion depth in X direction');

[X,Y]= meshgrid(Cz,Cx);  %make 2 matrices containing repeating rows or
columns of the original vectors so they may be multiplied together to
create a final visual of the 2D index profile
Z= X.*Y;

n_profile= nsub+ dn_pp/4*Z;   %from Almeida eq 9

figure()
set(gca,'FontSize',14)
imagesc(n_profile); axis image                %visualize the index
profile, square pixels

set(gca,'xtick',[0 w/dd 2*w/dd 3*w/dd 4*w/dd 5*w/dd 6*w/dd])
set(gca,'XTickLabel',{'-3w','-2w','-w','0','w','2w','3w'})

title(['index distribution for mask window w=
',num2str(width),'\mum']);
```

```
xlabel([num2str(t),'hour anneal @',num2str(TC),'\circC']);
ylabel('Z Direction');

%now calculate 2D index profile

Dn_max= max(max(n_profile)) -nsub;
fprintf('\n\nExchange depth: %fum\nAnneal time: %2.1fh\nVertical
Diffusion: %f\nHorizontal Diffusion: %f\nSubstrate index: %f at
%1.3fum\nMax index change: %f\nda/de:
%f',h,t,dx+h,dz,nsub,lambda,Dn_max,dx/h)

fprintf('\n\n****FOR FIMMWAVE****\nx: %f\ny: %f\nxx: %f\nyy: 0\nzz:
0\n\n',dz,dx+h,Dn_max)

% %% Anneal Diffusion Coeff and depth calcs
% % ---------- Almeida findings, Xcut diffusion
%
% K= 8.617385e-5; %Boltzman const, [eV/K]
% Dox= 22.0e12;  %x cut diffusion coeff[um^2/h],as reported by Almeida
% Hx= 1.77;  %eV

t= 0:0.1:5;
TC1= 400;                %Temperature vector
T1= TC1+ 273.15;         %temperature [K]
Dx= Dox*exp(-Hx/(K*T1));

da= 2*sqrt(Dx*t);        %anneal depth da(Da,T)
figure()
set(gca,'FontSize',14)
plot(t,da), grid on
Title(['H^+ proton diffusion depth in LiNbO3 for ',num2str(TC1),'\circC
anneal, x dir, from (Almeida,2007)']);
xlabel('Time t[h]');ylabel('Anneal Depth da [\mum]');

%close all;
```

MATLAB Code for Mode Profile Simulations

```
format long

% ################################################
% IMPORT VARIABLE FOR AMF FILE BEFORE RUNNING CODE
% Variable Name = test
% ################################################

A = test';
B = zeros(161,251);
C = zeros(161,251);
D = zeros(161,251);

% Find 1/e of maximum field strength
Emax = max(max(A));
thresh = Emax./exp(1);

% Find the maximum intensity (i.e. center of mode profile)
% Will be used later as a reference point
SigMax = find(A == Emax);

% Make another plot that is just 0,1 based on intensity
% 0<(1/e) and 1>=(1/e)
for r=1:1:161;
    for c=1:1:251;
        if A(r,c)<thresh;
            B(r,c)=0;
        else
            B(r,c)=1;
        end
    end
end

% Determine mode width and height based on intensity
Bx = sum(max(B));
By = sum(max(B'));

wX = Bx*(50/251);
wY = By*(25/161);
MFD = sqrt(wX*wY);

% Invert plot so it plots correctly
for i=1:1:161;
    C(i,:) = A(161-i+1,:);
    D(i,:) = B(161-i+1,:);
end

% Plot the mode profile, with mode data in the title
figure(1)
set(gca,'FontSize',14)
```

```
imagesc(0:50/251:50,0:25/161:25,C)
imagesc(C)
xlabel('Horizontal [\mum]')
ylabel('Vertical [\mum]')
title(sprintf('APE Mode Profile from Fimmwave\n%0.3f um (x) by %0.3f um
(y)\nMFD = %0.3f um',wX,wY,MFD))
grid on

figure(2)
set(gca,'FontSize',14)
imagesc(0:50/251:50,0:25/161:25,D)
imagesc(D)
xlabel('Horizontal [\mum]')
ylabel('Vertical [\mum]')
title(sprintf('APE Mode Profile from Fimmwave\n%0.3f um (x) by %0.3f um
(y)\nMFD = %0.3f um',wX,wY,MFD))
grid on

area = sum(sum(D)).*(50/251).*(25/161);


%% Figure out mode profile sigmas
% With widths known, figure out sigmas for mode profile
% Change the value of the maximum intensity
B(SigMax) = 1000;
% Find the maximum value in each row
Bmax_y = max(B');
% Find the index corresponding to each location
Bmax_y_first = find(Bmax_y == 1, 1, 'first');   % bottom edge of mode
profile
Bmax_y_last = find(Bmax_y == 1, 1, 'last');     % top edge of mode
profile
Bmax_y_max = find(Bmax_y == 1000, 1, 'first');  % maximum intensity
point

% Calculate the sigmas
sigma1 = abs(Bmax_y_last - Bmax_y_max).*(25/161) + (25/161)/2
sigma2 = abs(Bmax_y_first - Bmax_y_max).*(25/161) + (25/161)/2
sigma3 = wX/2


%% Calculate coupling loss with fiber
% Fiber 1/e^2 beam width
d = 10.7; %1/e diameter of fiber, um
a = d/2;

% Mode mismatch loss equation
eta = 2*( (a^-2 + sigma1^-2)^(-1/2) + (a^-2 + sigma2^-2)^(-1/2))^2/
(a^2*sigma3*(sigma1+sigma2)*(a^-2+sigma3^-2));
loss = -10*log10(eta);
MFD = sqrt(wX*wY);
```

```
fprintf('\n********** Mode Profile **********')
fprintf('\nMode field is %0.4f um (horizontal) x %0.4f um
(vertical)',wX,wY)
fprintf('\nMode area is %0.4f um^2',area)
fprintf('\n\nCoupling MFD is %0.4f um',MFD)
fprintf('\nMode mismatch factor is %0.4f',eta)
fprintf('\nMode mismatch loss is %0.4f dB\n\n',loss)
```

MATLAB Code for Measured Mode Profile Calculations

```
%% Read In Beam Profiler Data
clc
clear all
close all
format long

% Beam Profiler File
% Calibration WG 1
fid1 = 'C:\';
% Calibration WG 2
fid2 = 'C:\';
% Waveguide Separation [um]
sep = 125;

% Waveguide Under Test
fid3 = 'C:\';


%% Read In Reference Files
% First Reference Files
% Read in beam profiler file, ignoring header information (first 39
lines)
% Split into each individual column
C = csvread(fid1,39,0);
x = C(:,1);
x1n = x;
Ex = C(:,2);
y = C(:,3);
y1n = y;
Ey = C(:,4);

% Normalize intensity
Ex= Ex/max(Ex);
Ex1n = Ex;
Ey= Ey/max(Ey);
Ey1n = Ey;

% Limit for FWHM (3dB point reference)
e_lim(1:length(x))= exp(-2);

% Find intersection of intensity and 1/e^2 for x-dimension
Ex1 = abs(Ex-exp(-2)); %plot zero crossing at 1/e^2 placements
Ey1 = abs(Ey-exp(-2));
[Ex_max1,Ex_imax1] = max(Ex);  %find maximum x location
[x_min1,x_i1] = min( Ex1(1:Ex_imax1)); %find 1/e^2 location between 0
and Ex_max
[x_min2,x_i2] = min( Ex1(Ex_imax1:length(Ex))); %find 1/e^2 location
between Ex_max and last data point
x_i2 = x_i2+ Ex_imax1; %add center location index to second minimum
index
```

```
wEx1 = abs(x(x_i1)- x(x_i2)); %find 1/e^2(Ex) distance

% Find intersection of intensity and 1/e^2 for x-dimension
[Ey_max1,Ey_imax1] = max(Ey);  %find maximum y location
[y_min1,y_i1] = min( Ey1(1:Ey_imax1)); %find 1/e^2 location between 0
and Ey_max
[y_min2,y_i2] = min( Ey1(Ey_imax1:length(Ey))); %find 1/e^2 location
between Ey_max and last data point
y_i2 = y_i2+ Ey_imax1; %add center location index to second minimum
index
wEy1 = abs(y(y_i1)- y(y_i2)); %find 1/e^2(Ey) distance

% Plot the intensity
[Ex_min1,Ex_imin1] = min(abs(Ex1));
[Ey_min1,Ey_imin1] = min(abs(Ey1));
peakRef1 = x(Ex_imax1);

%
**************************************************************************
*
% Second Reference File
% Read in beam profiler file, ignoring header information (first 39
lines)
% Split into each individual column
C = csvread(fid2,39,0);
x = C(:,1);
x2n = x;
Ex = C(:,2);
y = C(:,3);
y2n = y;
Ey = C(:,4);

% Normalize intensity
Ex= Ex/max(Ex);
Ex2n = Ex;
Ey= Ey/max(Ey);
Ey2n = Ey;

% Limit for FWHM (3dB point reference)
e_lim(1:length(x))= exp(-2);

% Find intersection of intensity and 1/e^2 for x-dimension
Ex1 = abs(Ex-exp(-2)); %plot zero crossing at 1/e^2 placements
Ey1 = abs(Ey-exp(-2));
[Ex_max2,Ex_imax2] = max(Ex);  %find maximum x location
[x_min1,x_i1] = min( Ex1(1:Ex_imax2)); %find 1/e^2 location between 0
and Ex_max
[x_min2,x_i2] = min( Ex1(Ex_imax2:length(Ex))); %find 1/e^2 location
between Ex_max and last data point
x_i2 = x_i2+ Ex_imax2; %add center location index to second minimum
index
wEx2 = abs(x(x_i1)- x(x_i2)); %find 1/e^2(Ex) distance
```

```
% Find intersection of intensity and 1/e^2 for x-dimension
[Ey_max2,Ey_imax2] = max(Ey);  %find maximum y location
[y_min1,y_i1] = min( Ey1(1:Ey_imax2)); %find 1/e^2 location between 0
and Ey_max
[y_min2,y_i2] = min( Ey1(Ey_imax2:length(Ey))); %find 1/e^2 location
between Ey_max and last data point
y_i2 = y_i2+ Ey_imax2; %add center location index to second minimum
index
wEy2 = abs(y(y_i1)- y(y_i2)); %find 1/e^2(Ey) distance

% Plot the intensity
[Ex_min2,Ex_imin2] = min(abs(Ex1));
[Ey_min2,Ey_imin2] = min(abs(Ey1));
peakRef2 = x(Ex_imax2);

%
**************************************************************************
*
% Find Resolution from Reference Files
umPP = sep/abs(peakRef2 - peakRef1)


%% Read in waveguide under test
%
**************************************************************************
*
% Second Reference File
% Read in beam profiler file, ignoring header information (first 39
lines)
% Split into each individual column
C = csvread(fid3,39,0);
x = C(:,1);
x3n = x;
Ex = C(:,2);
y = C(:,3);
y3n = y;
Ey = C(:,4);

% Normalize intensity
Ex= Ex/max(Ex);
Ex3n = Ex;
Ey= Ey/max(Ey);
Ey3n = Ey;

% Limit for FWHM (3dB point reference)
e_lim(1:length(x))= exp(-2);

% Find intersection of intensity and 1/e^2 for x-dimension
Ex1 = abs(Ex-exp(-2)); %plot zero crossing at 1/e^2 placements
Ey1 = abs(Ey-exp(-2));
[Ex_max3,Ex_imax3] = max(Ex);  %find maximum x location
```

```
[x_min1,x_i1] = min( Ex1(1:Ex_imax3)); %find 1/e^2 location between 0
and Ex_max
[x_min2,x_i2] = min( Ex1(Ex_imax3:length(Ex))); %find 1/e^2 location
between Ex_max and last data point
x_i2 = x_i2+ Ex_imax3; %add center location index to second minimum
index
wEx3 = abs(x(x_i1)- x(x_i2)); %find 1/e^2(Ex) distance

% Find intersection of intensity and 1/e^2 for x-dimension
[Ey_max3,Ey_imax3] = max(Ey);  %find maximum y location
[y_min1,y_i1] = min( Ey1(1:Ey_imax3)); %find 1/e^2 location between 0
and Ey_max
[y_min2,y_i2] = min( Ey1(Ey_imax3:length(Ey))); %find 1/e^2 location
between Ey_max and last data point
y_i2 = y_i2+ Ey_imax3; %add center location index to second minimum
index
wEy3 = abs(y(y_i1)- y(y_i2)); %find 1/e^2(Ey) distance

% Plot the intensity
[Ex_min3,Ex_imin3] = min(abs(Ex1));
[Ey_min3,Ey_imin3] = min(abs(Ey1));


%% Plot Modes with Correct Scaling

% First file
sigma11= abs(y1n(Ey_imax1)-y1n(Ey_imin1));
sigma21= wEy1 - sigma11;

wX1 = wEx1.*umPP;
wY1 = wEy1.*umPP;
s11 = sigma11*umPP;
s21 = sigma21*umPP;
s31 = wX1/2;

% Second file
sigma12= abs(y2n(Ey_imax2)-y2n(Ey_imin2));
sigma22= wEy2 - sigma12;

wX2 = wEx2.*umPP;
wY2 = wEy2.*umPP;
s12 = sigma12*umPP;
s22 = sigma22*umPP;
s32 = wX2/2;

% Third file
sigma13= abs(y3n(Ey_imax3)-y2n(Ey_imin3));
sigma23= wEy3 - sigma13;

wX3 = wEx3.*umPP;
wY3 = wEy3.*umPP;
s13 = sigma13*umPP;
```

```
s23 = sigma23*umPP;
s33 = wX3/2;

% Fiber 1/e^2 beam width
d = 10.7; %1/e diameter of fiber, um
a = d/2;

eta1 = 2*( (a^-2 + s11^-2)^(-1/2) + (a^-2 + s21^-2)^(-1/2))^2/
(a^2*s31*(s11+s21)*(a^-2+s31^-2));
loss1 = -10*log10(eta1);
MFD1 = sqrt(wX1*wY1);

eta2 = 2*( (a^-2 + s12^-2)^(-1/2) + (a^-2 + s22^-2)^(-1/2))^2/
(a^2*s32*(s12+s22)*(a^-2+s32^-2));
loss2 = -10*log10(eta2);
MFD2 = sqrt(wX2*wY2);

eta3 = 2*( (a^-2 + s13^-2)^(-1/2) + (a^-2 + s23^-2)^(-1/2))^2/
(a^2*s33*(s13+s23)*(a^-2+s33^-2));
loss3 = -10*log10(eta3);
MFD3 = sqrt(wX3*wY3);

fprintf('\n********** First File **********')
fprintf('\nMode field is %0.4f um (horizontal) x %0.4f um
(vertical)',wX1,wY1)
fprintf('\n\nCoupling MFD is %0.4f um',MFD1)
fprintf('\nMode mismatch factor is %0.4f',eta1)
fprintf('\nMode mismatch loss is %0.4f dB',loss1)


fprintf('\n\n\n********** Second File **********')
fprintf('\nMode field is %0.4f um (horizontal) x %0.4f um
(vertical)',wX2,wY2)
fprintf('\n\nCoupling MFD is %0.4f um',MFD2)
fprintf('\nMode mismatch factor is %0.4f',eta2)
fprintf('\nMode mismatch loss is %0.4f dB',loss2)


fprintf('\n\n\n********** Third File **********')
fprintf('\nMode field is %0.4f um (horizontal) x %0.4f um
(vertical)',wX3,wY3)
fprintf('\n\nCoupling MFD is %0.4f um',MFD3)
fprintf('\nMode mismatch factor is %0.4f',eta3)
fprintf('\nMode mismatch loss is %0.4f dB\n\n',loss3)


%% Sample plot
figure(5)
ds=5; %downsample scale factor
x1= 1:length(Ex1n);
x2=1:ds:length(Ex1n);
```

```
Ex_int= interp1(x1,Ex1n,x2);
Ey_int= interp1(x1,Ey1n,x2);
[X,Y]= meshgrid(Ex_int,Ey_int);
Y1=Y(length(Y):-1:1,length(Y):-1:1);
Z= X.*Y1;
imagesc(Z), %axis image
title('First calibration file')

figure(6)
ds=5; %downsample scale factor
x1= 1:length(Ex2n);
x2=1:ds:length(Ex2n);
Ex_int= interp1(x1,Ex2n,x2);
Ey_int= interp1(x1,Ey2n,x2);
[X,Y]= meshgrid(Ex_int,Ey_int);
Y1=Y(length(Y):-1:1,length(Y):-1:1);
Z= X.*Y1;
imagesc(Z), %axis image
title('Second calibration file')

figure(7)
ds=5; %downsample scale factor
x1= 1:length(Ex3n);
x2=1:ds:length(Ex3n);
Ex_int= interp1(x1,Ex3n,x2);
Ey_int= interp1(x1,Ey3n,x2);
[X,Y]= meshgrid(Ex_int,Ey_int);
Y1=Y(length(Y):-1:1,length(Y):-1:1);
Z= X.*Y1;
imagesc(Z), %axis image
title('Waveguide under test')
```

VITA

Name:	Dwayne Denton Macik
Address:	Department of Electrical and Computer Engineering, Texas A&M University, 214 Zachry Engineering Center, TAMU 3128 College Station, TX 77843-3128
Email Address:	dmacik@tamu.edu
Education:	B.S., Electrical Engineering, Texas A&M University, 2010 M.S., Electrical Engineering, Texas A&M University, 2012